

Polymer blends for light-outcoupling management in organic light-emitting diodes

Polymerblends für Lichtauskopplungsmanagement in organische Leucht-dioden

Wissenschaftliche Arbeit zur Erlangung des Grades

Master of Science

an der Fakultät für Chemie der Technischen Universität München

Betreut von Professor Dr. Bernhard Rieger
Wacker-Lehrstuhl für Makromolekulare Chemie
und Dr. Gert-Jan Wetzelaer
Max-Planck-Institut für Polymerforschung

Eingereicht von Sipeng Liu
(München)

Eingereicht am Garching, den 30. September 2021

Abstract

The internal quantum efficiency of organic light-emitting diodes (OLEDs) can now reach ~100% by using phosphorescent emitters. However, the extraction of photons remains rather inefficient (typically <30%), due to the intrinsic multi-layer device structure and the mismatch of refractive indices. It is known that reducing the refractive indices of the constituent layers in an OLED can enhance light extraction. Since poly(3,4-ethylenedioxythiophene):poly (styrene sulfonate) (PEDOT:PSS) has relative good electrical conduction and can be solution processed and has also been widely used as a hole-conducting polymer in OLEDs, it was chosen to be investigated in this work. This thesis introduces two approaches to reduce the refractive index of PEDOT:PSS layer, i.e., by blending with fluorinated polymeric nanoparticles and the formation of porosity in the layer. Furthermore, we fabricated and characterized OLEDs integrated with modified PEDOT:PSS layers, demonstrating similar external quantum efficiency which is due to the small effect the refractive index of the hole transport layer has on the outcoupling efficiency.

Zusammenfassung

Die interne Quanteneffizienz von organischen Leuchtdioden (OLEDs) kann durch die Verwendung von phosphoreszierenden Emittern inzwischen ~100 % erreichen. Die Extraktion von Photonen ist jedoch nach wie vor recht ineffizient (typischerweise <30 %), was auf die inhärente Mehrschichtstruktur des Geräts und die Fehlanpassung der Brechungsindizes zurückzuführen ist. Es ist bekannt, dass eine Verringerung der Brechungsindizes der einzelnen Schichten in einer OLED die Lichtausbeute verbessern kann. Da PEDOT:PSS eine relativ gute elektrische Leitfähigkeit aufweist, in Lösung verarbeitet werden kann und auch als lochleitendes Polymer in OLEDs weit verbreitet ist, wurde es für die Untersuchung in dieser Arbeit ausgewählt. In dieser Arbeit werden zwei Ansätze zur Verringerung des Brechungsindex der PEDOT:PSS-Schicht vorgestellt, nämlich die Vermischung mit fluorierten polymeren Nanopartikeln und die Bildung von Porosität in der Schicht. Darüber hinaus haben wir OLEDs mit modifizierten PEDOT:PSS-Schichten hergestellt und charakterisiert, die eine ähnliche externe Quanteneffizienz aufweisen, was auf den geringen Einfluss des Brechungsindex der Lochtransportschicht auf die Auskopplungseffizienz zurückzuführen ist.

Contents

1. Introduction	1
2. Literature Review	3
3. Basics of Organic Light-emitting Diodes	7
3.1. Working principles and device structures	7
3.2. Device characterization	9
3.2.1. Internal and external quantum efficiency	9
3.2.2. Current efficiency	10
3.2.3. Power efficiency	10
3.2.4. Color rendering and quality	10
3.2.5. Angular dependent emission	12
3.3. Key factors to enhancement in EQE	12
3.3.1. Refractive index	12
3.3.2. Emitter orientation	14
3.4. Optical loss channels	16
4. Materials and Methods	18
4.1. Materials	18
4.2. Synthesis of polymeric nanoparticles dispersion	18
4.3. Si substrate cleaning	19
4.4. Glass/ITO substrates cleaning	19
4.5. Preparation of Porous PEDOT:PSS layer	19
4.6. Preparation of SYPPV solution	20
4.7. OLEDs fabrication	20
4.8. Dynamic light scattering (DLS) measurement	20
4.9. Thermogravimetric analysis (TGA)	21
4.10. Surface tension measurement	21

4.11.	Refractive index measurement	21
4.12.	Transmission measurement	23
4.13.	Atomic force microscopy (AFM) measurement.....	23
4.14.	Thickness measurement	23
4.15.	Current density-voltage-luminescence measurement.....	23
4.16.	Electroluminescence measurement.....	24
5.	Results and Discussion	25
5.1.	Modification of PEDOT:PSS layer	25
5.1.1.	Blending with fluorinated polymeric nanoparticles.....	25
5.1.2.	Formation of porous structure	30
5.2.	OLEDs integrated with modified PEDOT:PSS layers	33
6.	Conclusions and Outlook	37
7.	References	39
	List of Figures	46
	List of Tables	48
A.	Appendix.....	49
B.	Acknowledgements.....	51
C.	Statement of Authorship	52

Acronyms and Abbreviations

4H-PFDA	1H,1H,2H,2H-perfluorodecyl acrylate
AFM	Atomic force microscope
CIE	Commission Internationale de L'Eclairage
DLS	Dynamic light scattering
EBL	Electron blocking layer
EIL	Electron injection layer
EL	Electroluminescence
EMA	Effective medium approximation
EML	Emissive layer
EQE	External quantum efficiency
ETL	Electron transport layer
HBL	Hole blocking layer
HIL	Hole blocking layer
HOMO	Highest occupied molecular orbital
HTL	Hole transport layer
IQE	Internal quantum efficiency
ITO	Indium tin oxide
LUMO	Lowest unoccupied molecular orbital
MSE	Mean square error
NP	Nanoparticle
PEDOT	Poly(3,4-ethylenedioxythiophene)
PFOS	Perfluorooctanesulfonic acid
PFPA	Pentafluorophenyl acrylate
PMMA	Poly(methyl methacrylate)
PS	Polystyrene
PSS	Poly(styrene sulfonate)
RMS	Root-mean-square
SDS	Sodium dodecyl sulfate
SPP	Surface plasmon polariton
SYPPV	Super yellow poly(p-phenylene vinylene)
TADF	Thermally activated delayed fluorescence

TDMV	Transition dipole moment vector
TE	Transverse-electric
TEWG	Transverse electric waveguide
TGA	Thermogravimetric analysis
TIR	Total internal reflection
TM	Transverse-magnetic
V59	2,2'-Azobis(2-methylbutyronitrile)
VASE	Variable angle spectroscopic ellipsometry

1. Introduction

Since first demonstrated by Tang and VanSlyke in 1987 ^[1], organic light-emitting diodes (OLEDs) have undergone rapid development and progress. For over three decades, the efficiency, brightness, and stability of OLEDs have improved dramatically. Nowadays, the OLED technology has matured to be applied in display and lighting industries. For both applications, device efficiency is the key requirement, since it not only relates to the power conversion from electricity to light, but also the losses lead to heating which may thus cause rapid device degradation. Mostly thanks to the development of triplet harvesting emissive layers,^[2–4] doped charge transport layers,^[5,6] and efficient charge blocking structures,^[7] the internal quantum efficiency (IQE) of OLEDs has now been reached unity in many state-of-the-art devices. However, only a small fraction of generated photons can escape the multilayer device structure of OLEDs. The external quantum efficiency (EQE) remains below 30% for a typical OLED, which can be attributed to the different optical loss channels in the device responsible for the reduced fraction of generated light emitted into air.

Loss channels that limit the performance of OLEDs are absorption, surface plasmon polaritons (SPPs), and waveguiding in the substrate or the organic layers. Trapped photons in the substrate can be efficiently extracted by external outcoupling structures on the backside of the glass, but if one wants to extract waveguided modes from the organic layers or SPP modes, internal outcoupling features are necessary. Internal scattering structures are mainly used, but those often require additional extensive and expensive fabrication steps. The other alternative approach to enhance light extraction is reducing the refractive indices of the constituent layers in an OLED. It has already been shown that EQE of (air + substrate) modes can be maximized reached ~90% when refractive indices of anode, hole transport layer (HTL), emissive layer (EML), and electron transport layer (ETL) are lowered to 1.5.^[8]

As the conducting polymer poly(3,4-ethylenedioxythiophene):poly(styrene sulfonate) (PEDOT:PSS) has shown water-solubility, a promising electrical

conductivity and an exceptional environmental stability, PEDOT:PSS has been widely used as a hole injecting layer/hole transport layer (HIL/HTL) in OLEDs. In this work, we present two approaches to reduce the refractive index of PEDOT:PSS layer, i.e., by blending PEDOT:PSS with fluorinated polymeric nanoparticles possessing a lower refractive index and introducing voids in the layer by spin-coating PEDOT:PSS/Polystyrene (PS) latex mixture, followed by selectively removing PS particles. By this two methods, the refractive index of PEDOT:PSS layer can be reduced from 1.54 to 1.42 and 1.36, respectively. Furthermore, OLED devices integrated with the modified PEDOT:PSS layers were fabricated. Compared to the reference device, similar EQE was found. Based on the optical simulation, this is due to the small effect the refractive index of the hole transport layer has on the outcoupling efficiency.

2. Literature Review

The first passage of this literature review presents various publications on additional external features to extract light contained inside the substrate of OLEDs. The second section focuses on the applied internal features which can enhance the outcoupling efficiency. In the last passage, publications regarding manipulating refractive index in OLEDs both in modelling and practical ways will be discussed. Before reviewing the following literature for this work, it is necessary to clarify that only bottom-emitting OLEDs are considered in this part.

A considerable amount of research dealing with extraction of substrate modes has been published. External outcoupling structures, that are applied onto the backside of the substrate of OLED devices, are often used to extract the light trapped in the substrate of the device. Similar to LEDs, ideally a hemisphere structure,^[9–12] matching the refractive index of substrate, with dimensions much greater than the active area of the OLED can be applied so that the source of light can be treated as a point source. As shown in

Figure 2.1 (a)^[13], this configuration allows all the light in the substrate to escape to air, since it propagates in the direction of surface normal. However, such macro-extractor structures^[12,14] are generally considered impractical for large OLED lighting panels while they are too bulky. Many micro/nano structures such as microlens^[15–19] (Figure 2.1 (b)) and pyramids^[20] arrays, applied to the backside of OLED substrates have also been reported. Such structures can recover a large fraction of the substrate mode via reducing total internal reflection (TIR), improvements in outcoupling efficiency by factors ranging from 1.5 to 1.7 have been reached.^[19–22] In addition, depositing a scattering layer on the backside of the substrate or roughening the back-surface of the substrate can also enhance the outcoupling efficiency due to scattering.^[23–25] As shown in Figure 2.1 (c), T. Koh *et al.* developed a thin porous scattering layer to improve the outcoupling efficiency.^[23] With this scattering layer integrated into a green OLED stack, a 65% enhancement of EQE and a 77% enhancement of the power efficiency was achieved.

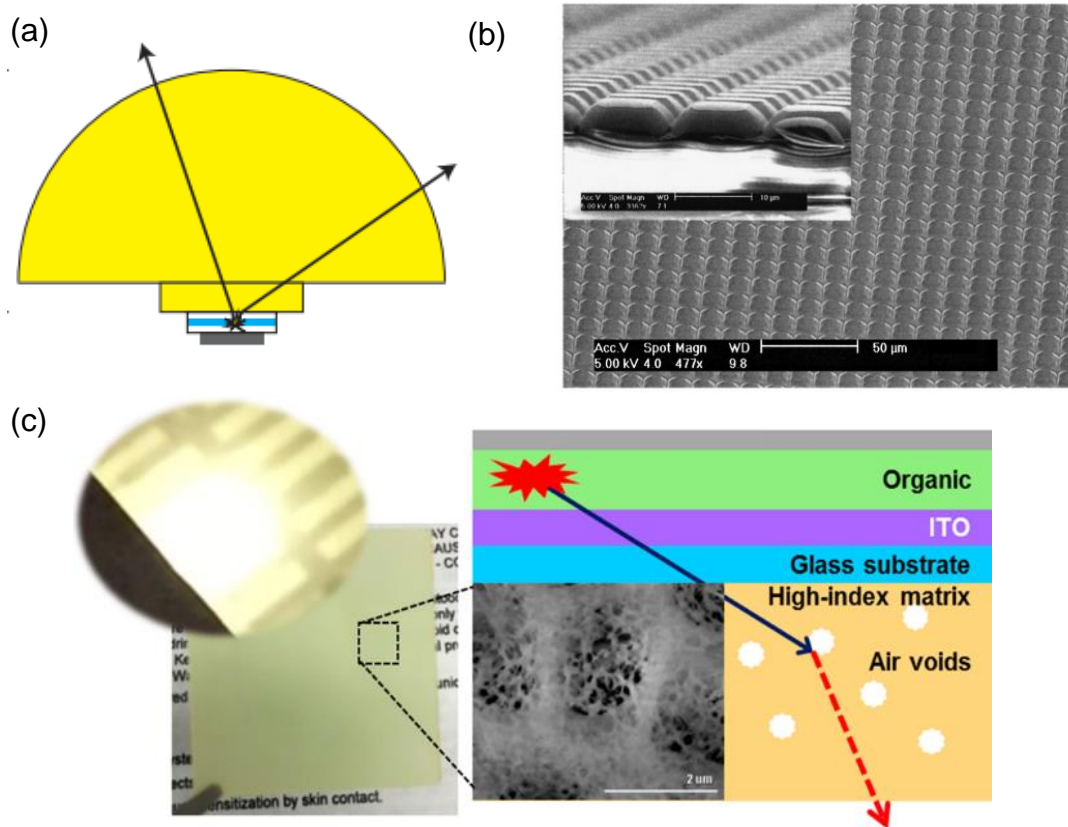


Figure 2.1. (a)^[13] Application of a macroextractor matching the refractive index of the substrate used. Here all photons in the substrate can escape to the air. (b)^[19] Scanning electron micrograph of microlens array with detailed side view of the base lens as an inset. (c)^[23] A schematic illustration of a light scattering layer employing air voids as scattering centers embedded in a high-index matrix for outcoupling the substrate mode.

In addition to the substrate mode, around 50% of light are trapped in waveguide and surface plasma polariton (SPP) mode in conventional OLEDs. In order to extract these two modes, internal outcoupling features are necessary.^[26–29] Internal periodic^[27,30,31] or random patterns^[26,32,33] are mainly used, typically forming a corrugated or buckled OLED structure, which shows a similar effect to scattering. As shown in Figure 2.2, Koh *et al.* introduced an indium tin oxide (ITO) grid-based approach to extract the waveguide mode.^[31] To introduce a contrast in refractive index, the ITO structure is capped with the low refractive index conductive polymer PEDOT:PSS. Due to the truncated pyramidal shape of the ITO electrode and the contrast in refractive index, a fraction of light originally limited in waveguide modes is redirected and become able to escape to air. It should be noted that while the tapered ITO grid was fabricated by conventional photolithography techniques, the size of this microstructure and the taper angle can be tuned to optimize the efficiency of this approach.

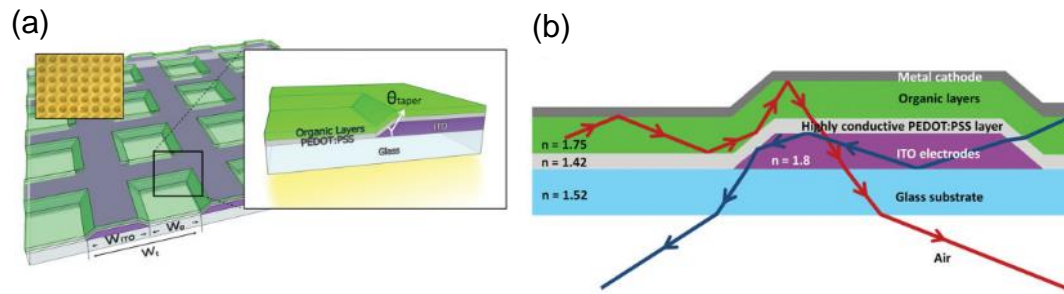


Figure 2.2.^[31] Schematic illustration of a patterned ITO with the low-index conductive PEDOT:PSS used to extract light from waveguide mode in an OLED. (a) 3D scheme of the Structure. (b) Cross-sectional view of the structure indicating selected light paths.

However, those internal structures always require additional extensive and expensive fabrication steps,^[28] and can make devices prone to the electrical short-circuit and local high-field induced degradation.^[34,35] Therefore, this could be a significant hurdle in applying those technologies in real-world applications. An alternative way to extract waveguide and SPP modes is reducing the refractive indices of the constituent layers in an OLED.^[8,36–39] Salehi *et al.* calculated the maximum achievable EQE extracted to air (η_A) and to “air + substrate” (η_{A+S}) for 11 different cases with varied refractive indices, as presented in Table 2.1.^[8] It is shown in device A that decreasing the refractive indices of anode, HTL, EML and ETL to 1.5 (i.e., matching the refractive index of glass substrate), can lead to an extraction efficiency of 87.8% into the substrate and air due to the elimination of waveguide modes and the suppression of SPP modes. Comparing the other devices, one can find that decreasing the refractive index of HTL, ETL or ITO results in an enhancement in outcoupling efficiency. According to the SPP dispersion equation, the SPP mode dispersion and the refractive index of the layer adjacent to the metal cathode are negatively correlated.^[40–42] Thus, an ETL with lower refractive index will suppress the loss to SPPs.^[37,39] The refractive indices of HTL and transparent anode are theoretically expected to have large impact on transverse electric waveguide (TEWG) mode, as reported by Salehi *et al.*^[43] Therefore, the increase of outcoupling efficiency via lowering the refractive indices of HTL and anode origins from the extraction of TEWG mode. Experimentally, Umbach *et al.* modified the active HTL to have a significantly reduced refractive index using electrospray deposition.^[44] A green-emitting

OLED stack integrated with this modified HTL achieved a maximum increase of 10% in outcoupling efficiency. Lu *et al.* reported above 60% EQE was achieved by replacing the ITO (refractive index ~ 2.1) electrode with PEDOT:PSS (refractive index ~ 1.5). Many other works on ITO-free OLEDs with higher EQE were also published.^[45–48] As aspect of materials with low refractive index, instead synthesizing new compounds several approaches based on the well-known functional materials used in OLEDs were proposed. For instance, the refractive index of a functional layer in OLEDs can be lowered by mixing with other materials possessing a lower refractive index physically^[49–52] or chemically (like copolymerization^[53]), or by forming a porous structure (i.e., introducing voids into the layer) using oblique angle deposition^[8,54–56] or electrospray deposition^[44]. It is noteworthy that the impact of these modifications on the electrical and optical properties should also be taken into account.

Table 2.1.^[8] Maximum Achievable Air (η_A) and Air + Substrate (η_{A+S}) EQEs^a

case	reference device	device A	device B	device C	device D	device E	device F	device G	device H	device I	device J
refractive index of anode (ITO)	2.1	<u>1.5</u>	<u>2.0</u>	2.1	2.1	<u>1.5</u>	<u>2.0</u>	2.1	2.1	2.1	2.1
refractive index of HTL (TAPC)	1.68	<u>1.5</u>	<u>2.0</u>	1.68	1.68	1.68	1.68	<u>1.5</u>	<u>2.0</u>	1.68	1.68
refractive index of EML (CBP)	1.8	<u>1.5</u>	<u>2.0</u>	1.8	1.8	1.8	1.8	1.8	1.8	<u>1.5</u>	<u>2.0</u>
refractive index of ETL (Alq3)	1.75	<u>1.5</u>	<u>2.0</u>	<u>1.5</u>	<u>2.0</u>	1.75	1.75	1.75	1.75	1.75	1.75
max achievable air (η_A)	31.6%	32.5%	21.0%	38.4%	25.2%	26.6%	31.0%	36.6%	25.0%	28.5%	32.5%
max achievable air + substrate (η_{A+S})	63.1%	87.8%	43.4%	73.2%	50.7%	69.4%	63.2%	63.0%	51.7%	59.4%	63.7%

^aMaximum achievable air (η_A) and air + substrate (η_{A+S}) for optically optimized OLED devices. All devices have the following structures: ITO (100 nm)/TAPC (optically optimized thickness)/CBP-Irppy₂acac (20 nm)/Alq₃ (optically optimized thickness)/aluminum (100 nm). For the reference device, the following indices of refraction are used: $n_{ITO} = 2.1$, $n_{TAPC} = 1.68$, $n_{CBP} = 1.8$, and $n_{Alq_3} = 1.75$ at 525 nm. To evaluate the effect of refractive index, η_A and η_{A+S} are calculated using different values of indices of refraction (under lined in the table) for different cases.

3. Basics of Organic Light-emitting Diodes

This chapter focuses on the fundamentals of organic light-emitting diodes (OLEDs). First, a brief introduction is presented about the working principles and the general structures of OLEDs. Basic concepts are then covered in relation to the performance of the OLED devices. Two key factors for outcoupling efficiency enhancement are mentioned in the next section. The last part focuses on the optical loss channels of the OLEDs.

3.1. Working principles and device structures

OLEDs are ultrathin light sources made of thin-film organic semiconductors sandwiched between two electrodes. The process of light generation in a basic OLED under operation is schematically illustrated in Figure 3.1.^[57] An external driving voltage of typically a few volts is applied to the OLED device so that holes and electrons are injected from anode and cathode, respectively. The holes and electrons migrate towards each other till they meet in the emissive layer (EML) to form excitons, which then may decay radiatively and emit photons due to recombination. In order to inject the electrons and the holes efficiently, a low barrier for holes (Δ_h) /electrons (Δ_e) is required in respect of the highest occupied molecular orbital (HOMO)/lowest unoccupied molecular orbital (LUMO) level of the organic material.

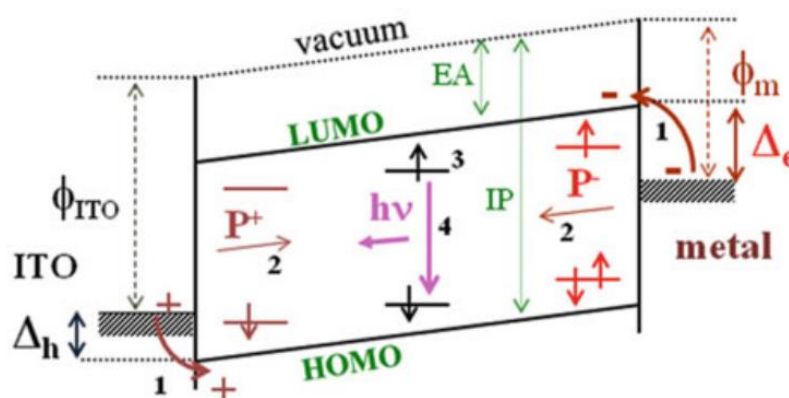


Figure 3.1.^[57] Scheme of the main steps involved in the process of light emission in an OLED: (1) charge injection from the electrodes, (2) charge transport, (3) exciton formation, and (4) exciton radiative recombination.

In order to obtain high efficiency, OLEDs are designed with a complex multilayer structure (Figure 3.2), in which each layer has a distinct function. These functional layers including the hole injection layer (HIL), hole transport layer (HTL), electron blocking layer (EBL), hole blocking layer (HBL), electron transport layer (ETL), and electron injection layer (EIL) have been inserted between the electrodes and EML to optimize the device performance.^[58–60] Here, the injection layers (HIL, EIL) facilitate the charge injection from the electrodes by decrease the energy barrier and the driving voltage,^[61,62] while transport layers (HTL, ETL) favor the charges transport.^[5,63,64] The functions of blocking layers(HBL, EBL) are to prevent the leakage of the opposite type of charge carrier and to confine the excitons within the EML.^[65,66]

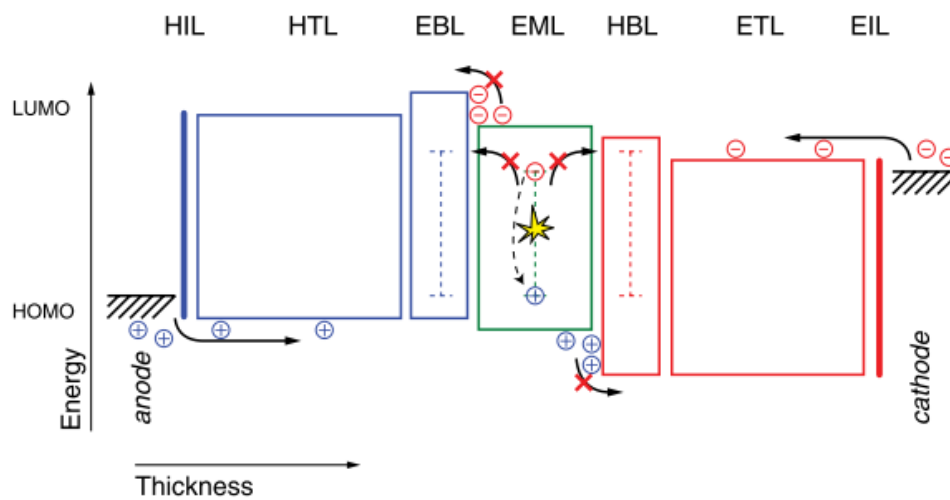


Figure 3.2.^[13] The energy diagram of a typical multilayer OLED. Boxes indicate the HOMO and LUMO levels of the materials.

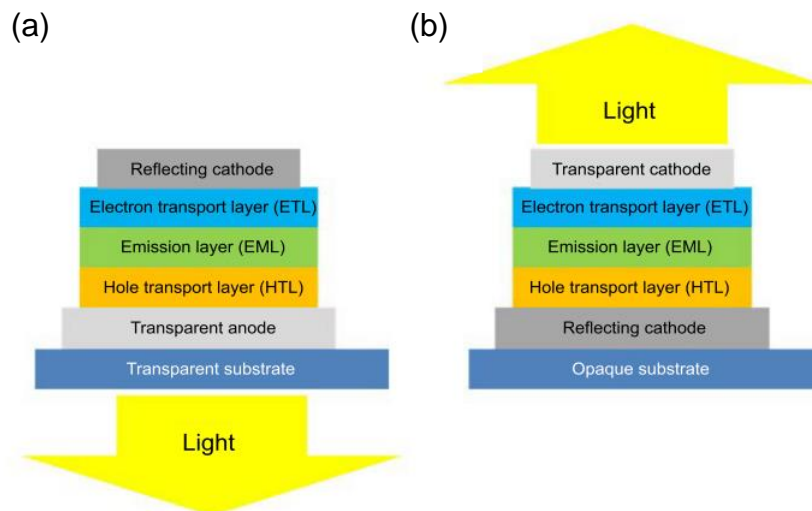


Figure 3.3.^[67] Schematic structures of (a) Bottom-emitting OLEDs. (b) Top-emitting OLEDs.

According to the emission direction relative to the substrate, OLEDs can be classified into bottom-emitting and top-emitting OLEDs, and their typical structure is shown in Figure 3.3. In conventional bottom-emitting devices, a transparent anode (typically ITO) is deposited on the transparent substrate, followed by organic layers and a highly reflective cathode. In contrast to bottom-emitting OLEDs, in top-emitting OLEDs a transparent cathode is required on the top of device so that the light is emitted in the top direction.

3.2. Device characterization

3.2.1. Internal and external quantum efficiency

The internal quantum efficiency (IQE, η_{int}), is defined as the ratio of the total number of photons generated within the OLED structure to the number of electrons injected.^[68] However, there is only a fraction of photons that can escape from the multilayer OLED structure. The external quantum efficiency (EQE, η_{ext}) is defined as the ratio of the number of photons emitted by the OLED into the viewing direction to the number of electrons injected.^[69] This means a large fraction of the light waveguided by the substrate (typically glass or plastics) and by the organic layers comprising the organic heterostructure, ultimately emerging out of the edge of the substrate, would be excluded during the EQE measurement. Based on the definitions, IQE and EQE differ by the fraction of light coupled out of the OLED into the viewing direction (η_{out}). Hence,

$$\eta_{\text{ext}} = \eta_{\text{int}} \eta_{\text{out}} \quad (3.1)$$

where η_{out} represents outcoupling efficiency.

Accurate measurement of the EQE of a OLED device can be achieved by measuring the total light output in the viewing direction and be calculated through Equation 3.2 reported by Forrest *et al.*^[69]

$$\eta_{\text{ext}} = \frac{\int \lambda I_{\text{detector}}(\lambda) d\lambda}{f I_{\text{OLED}} \int \lambda \eta_{\text{detector}}(\lambda) d\lambda} \quad (3.2)$$

Where I_{OLED} is the current passing through the OLED, I_{detector} is the incremental photocurrent generated in a photodetector placed on top of the OLED by the OLED power emitted at a center wavelength, λ , and η_{detector} is the external

quantum efficiency of the photodetector. As large aperture light collection optics are employed in the measurement, the wavelength dependence of f is small. Detailed calculations and measurements of EQE can be found in previous publications. ^[69,70]

3.2.2. Current efficiency

The current efficiency η_{CE} is defined as the ratio of luminance L [cd/m²] of the OLED to the current density J [A/m²]:

$$\eta_{CE} = \frac{L}{J} \left[\frac{\text{cd}}{\text{A}} \right] = \frac{AL}{I_{OLED}} \left[\frac{\text{cd}}{\text{A}} \right] \quad (3.3)$$

where A is the device active area. The current efficiency in candelas per ampère [cd/A] is widely used in the display industry.

3.2.3. Power efficiency

The power efficiency η_{PE} is described as the ratio of the emitted luminous flux ϕ [lm] to the total consumed electrical power P [W] externally required to drive the device:

$$\eta_{LE} = \frac{\phi}{P} \left[\frac{\text{lm}}{\text{W}} \right] = \frac{\phi}{UI} \left[\frac{\text{lm}}{\text{W}} \right] \quad (3.4)$$

where U represents the applied voltage.

The power efficiency is more related to the lighting field than the display application. Under the assumption of Lambertian distribution, for a device with an area of A , the luminous efficacy can be obtained with:

$$\eta_{LE} = \frac{\pi LA}{UI} \left[\frac{\text{lm}}{\text{W}} \right] \quad (3.5)$$

3.2.4. Color rendering and quality

To quantify the color, the human perception of light with different spectra should be taken into account. In 1931, a standard color coordinate (CIE coordinate) to quantify the color in a form of XYZ color space was created by the International Commission on Illumination (CIE). To eliminate the perception variation from

different viewers, the CIE defined the standard observer to represent as the average chromatic response of human beings.^[71] For the purpose of color measurement, the nature of human color vision has been quantified in terms of three color matching functions $x(\lambda)$, $y(\lambda)$ and $z(\lambda)$, as shown in Figure 3.4 (a). These color matching functions can be treated as the spectral sensitivity curves of three linear light detectors (human visibility), yielding the CIE tristimulus values of X , Y and Z ,^[72] respectively.

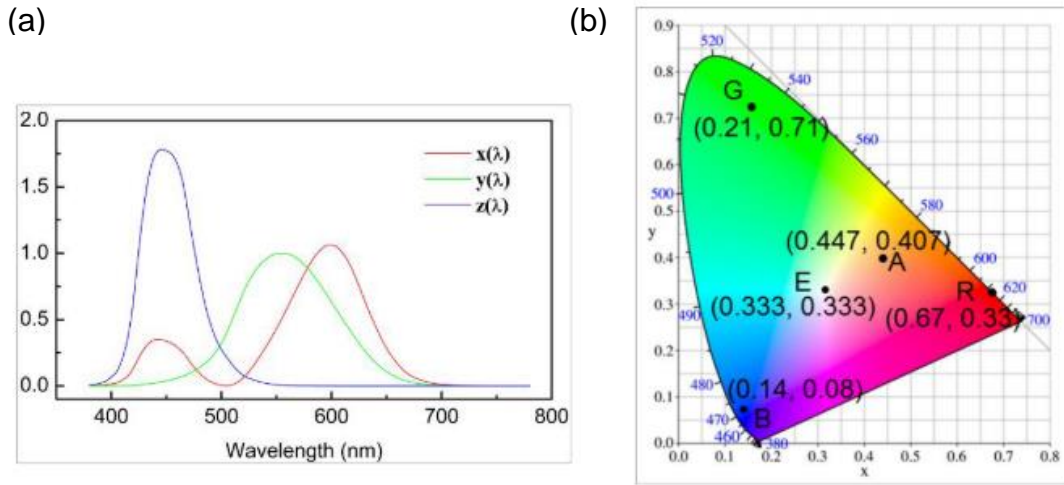


Figure 3.4.^[73] (a) Three color matching functions. (b) The CIE1931 xy chromaticity diagram. The points B, G and R represent primary blue, primary green and primary red according to the NTSC standard, respectively. The CIE coordinates A is the warm white and E is the cold white color.

In the emissive case, the CIE tristimulus values X , Y , Z can be obtained by:

$$X = \int_{\lambda} I(\lambda)x(\lambda)d\lambda, Y = \int_{\lambda} I(\lambda)y(\lambda)d\lambda, Z = \int_{\lambda} I(\lambda)z(\lambda)d\lambda \quad (3.6)$$

where the $I(\lambda)$ represents the spectral radiance of the light source within the visible wavelength from 380 nm to 780 nm.

The x , y , z coordinates in the CIE1931 chromaticity diagram then are given by:

$$x = \frac{X}{X+Y+Z}, y = \frac{Y}{X+Y+Z}, z = \frac{Z}{X+Y+Z} = 1 - x - y \quad (3.7)$$

The emitted color of OLEDs can be described by x and y in the two-dimensional CIE1931 chromaticity diagram, as shown in Figure 3.4 (b). Typically, the spectrum with a color coordinate (0.447, 0.407) at point A is referred to as the warm white. Meanwhile, the coordinate (0.333, 0.333) at point E is defined as

cold white.^[74] NTSC, named after the National Television System Committee in North America, is the most widely used color standard for the television color system. The original 1953 color NTSC standard, defined the colorimetric CIE coordinate values as follows: primary red R (0.67, 0.33), primary green G (0.21, 0.71) and primary blue B (0.14, 0.08). These typical points are also plotted in Figure 3.4 (b). In principle, all colors can be represented as the mixing of the primary blue, green and red with different coefficients.

3.2.5. Angular dependent emission

As discussed in Section 3.1, the basic structure of an OLED is like a sandwich, consisting of a bottom and top electrode forming a microcavity. The spectrum observed from different angles is dependent on the microcavity and the intrinsic emission of the emitter in free space.^[73] For general display and solid-state lighting applications, the color shift in different observing angles is unwanted. To quantify the angular dependent emission for an OLED, the variation of the electroluminescence spectrum and the CIE color coordinate at different observing angles should be recorded. Since the cavity leads to an inhomogeneous distribution of the electromagnetic energy radiated from OLEDs into the forward hemisphere, the distribution of radiance at different observation angles can be another parameter to describe the angular dependent emission for OLEDs.

3.3. Key factors to enhancement in EQE

3.3.1. Refractive index

The refractive index n of a material is a dimensionless number, describing how fast light propagate through the material. It is defined as

$$n = \frac{c}{v} \quad (3.8)$$

where c is the speed of light in vacuum, v is the phase velocity of light in the medium.

The refractive index determines how much the path of light is bent, or refracted,

when entering a material, which is described by Snell's law of refraction:

$$n_1 \sin \theta_1 = n_2 \sin \theta_2 \quad (3.9)$$

where θ_1 and θ_2 are the angles of incidence and refraction, respectively, of a ray crossing the interface between two media with refractive indices n_1 and n_2 . If there is no angle θ_2 fulfilling Snell's law, i.e., $\frac{n_1}{n_2} \sin \theta_1 > 1$, the light cannot be transmitted and will instead undergo total internal reflection (TIR). This occurs only when light goes to a material with lower refractive index, such as light propagates from glass substrate ($n \approx 1.5$) to air ($n = 1$). Based on the TIR phenomenon, the light can be extracted only when the angles of incidence θ_1 is smaller than the critical angle

$$\theta_c = \arcsin \left(\frac{n_1}{n_2} \right) \quad (3.10)$$

The refractive index is about 1.5 for the typical conventional glass and it is 1.7-1.8 for indium tin oxide (ITO) within the visible wavelength range. Additionally, the refractive index of the organic materials used for the functional layers in an OLED device is typically in range of 1.7-2.0 in the visible wavelength region. In a simple ray optical model (Figure 3.5) and assuming that light beam is initially emitted isotropically within the emissive layer (EML) of the device, one can estimate the outcoupling efficiency as

$$\eta_{out} \approx \frac{1}{2n^2} \quad (3.11)$$

where n is the refractive index of the emissive materials.

With $n \approx 1.8$, the η_{out} becomes approximately 15%. This rather low light outcoupling results from the mismatch of refractive index between the EML and the air. Only a fraction of light whose direction is within critical angle can be outcoupled to air ($n = 1$) due to total internal reflection. However, the $1/(2n^2)$ approximation is now generally considered to be an oversimplified estimation. For a modern and sophisticated model, anisotropic factor of emitter molecules, and the interactions between photons and each interface has to be taken into account.

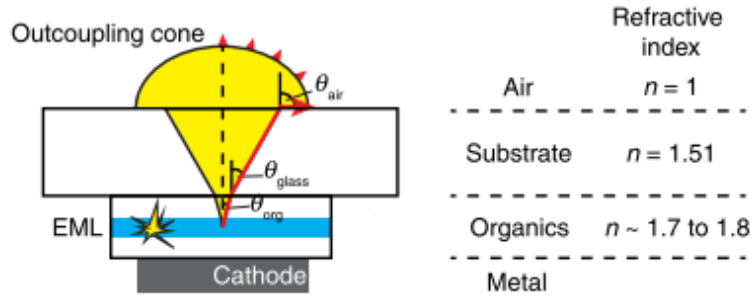


Figure 3.5.^[75] Illustration of refraction of the light emitted in the emissive layer (EML) of a bottom-emitting OLED. The outcoupling cone corresponds to the range of emission angles within the EML for which light can be extracted and is not trapped by total internal reflection.

3.3.2. Emitter orientation

In modern optical models, the emitting molecules/polymers in the OLED device are described as classical oscillating dipoles, which are illustrated in Figure 3.6.

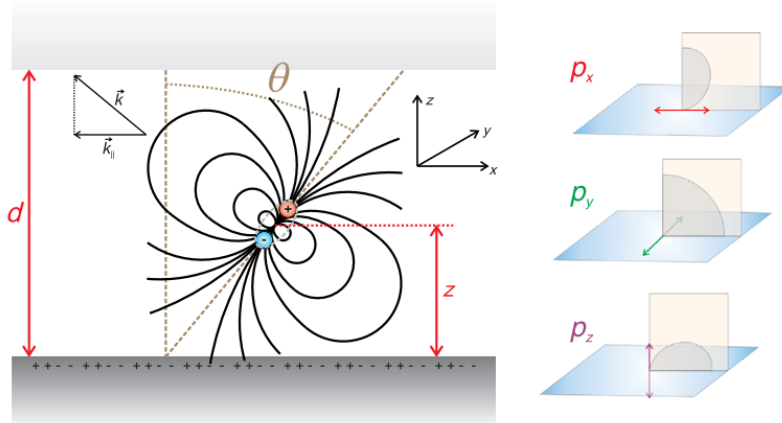


Figure 3.6.^[76] Schematic illustration of an oscillating electrical dipole embedded in a dielectric layer, which is sandwiched between two interfaces (a metal layer is located at the bottom). On the right side, the definition of the different emission polarizations is drawn.

In terms of emitter orientation, three distinct dipole orientations are determined with respect to the substrate (x-y plane)^[77,78].

- (i) $P_{\perp, TM}$: dipoles oriented perpendicular to the substrate plane (vertical, z direction), which emit p-polarized (transverse-magnetic (TM)) light.
- (ii) $P_{\parallel, TM}$: dipoles oriented parallel to the substrate plane (horizontal, x direction), which emit p-polarized light.

- (iii) $P_{\parallel,TE}$: dipoles oriented parallel to the substrate plane (horizontal, y direction), which emit s-polarized (transverse-electric (TE)) light.

The ensemble of emitting dipoles in an OLED emission layer is generally characterized using the anisotropy factor a :

$$a = \langle \cos^2 \theta \rangle \quad (3.3)$$

where $\langle \cos^2 \theta \rangle$ stands for the quadratic average of the projection of the transition dipole moment vectors (TDMVs) onto the surface normal. Thus, a completely horizontal distribution results in $a = 0$, an isotropic distribution (these three orientations weighted equally, i.e., $P_i = 1/3$) is described by $a = 1/3$, and a fully vertical orientation is given by $a = 1$.

The anisotropy factor a of emitters ensemble within the OLED device plays an important role in the outcoupling efficiency.^[79–81] A horizontally oriented dipole, with its axis lying in the substrate plane, leads to a maximum light extraction since a dipole's radiation is the strongest normal to its axis. A vertically oriented dipole will strongly couple to the TM-polarized SPP modes of the metallic cathode, since the SPP electric field will overlap with the dipole vector. Therefore, for highly efficient OLEDs, the TDMVs should preferentially align in the horizontal orientation with respect to the substrate plane^[82], since horizontally oriented dipoles would only very weakly couple to surface plasmon polaritons (SPPs).^[77,83] Figure 3.7. shows the effect of the emitter dipole orientation on mode contribution in an OLED.^[43]

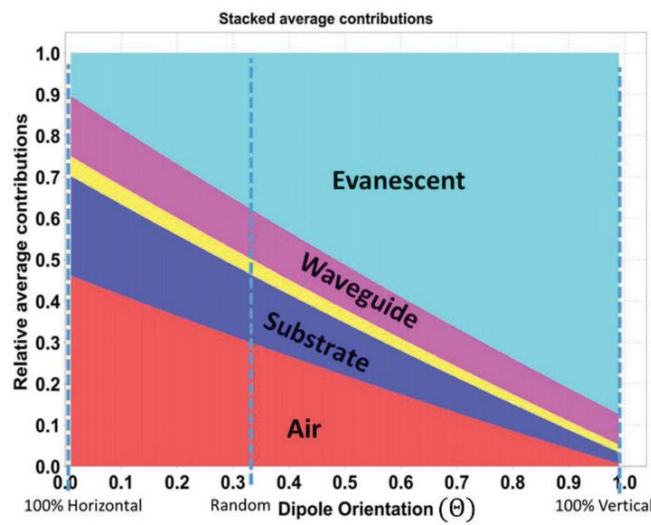


Figure 3.7.^[43] Effect of dipole orientation on mode-contribution in an OLED device. Vertically aligned dipole moments strongly couple to the surface plasmon polaritons and have a significant loss in the evanescent region.

3.4. Optical loss channels

In many state-of-the-art OLEDs, ~100% of IQE has been achieved due to optimized design and phosphorescent or thermally activated delayed fluorescent (TADF) emitters having a high photoluminescence quantum yield close to unity. The EQE of conventional OLEDs is still limited to 20%-30%, which is due to the multilayer structure of the OLED, introducing trapped light modes.

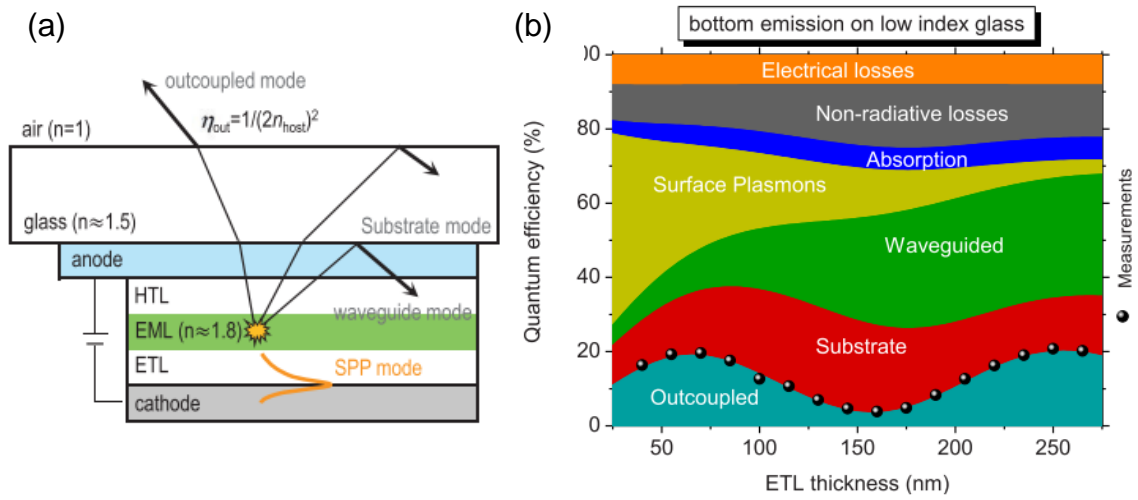


Figure 3.8. (a)^[42] Schematic diagram of the device structure of a bottom emitting OLED with ray tracing to demonstrate various modes in OLEDs, including outcoupled mode (air mode), substrate mode, waveguide mode and the excitation of SPP mode at the interface between the organic layer and the conductive metallic electrode. (b)^[84] Quantification of different loss channels for a red bottom emitting OLED as a function of the n-doped ETL thickness as predicted by optical modeling (established by Furno *et al.*^[78,85]).

Figure 3.8 (a) shows a scheme of an OLED's cross section, demonstrating the different light modes including air mode (outcoupled mode), substrate mode, waveguide mode and surface plasmon polariton (SPP) mode.^[86] Air mode represents the light generated in EML can be outcoupled into air. Substrate mode originates from the difference in refractive indices between air and glass substrate, leading to total internal reflection (TIR) at that interface. The losses due to TIR ($\theta_c = 41.5^\circ$) from substrate mode is comparable in energy at around 20%. Similar due to TIR, a noticeable portion of light with higher emission angles cannot even reach the glass substrate, but is waveguided in the organic layers (including the transparent indium tin oxide electrode) and ultimately lost

through absorption or edge emission, which is denoted as the waveguide mode. In addition to substrate and waveguide modes, the emitter dipoles can couple to the evanescent field of SPPs on the metal electrode propagating along the interface between the organic conductor layer and the metal electrode, which forms an SPP mode, resulting in severe losses in OLEDs. The fields of the SPP mode decay exponentially with distance. Thus, the efficiency of the emission is strongly decreased, if the EML is placed in the proximity of a metal layer. As shown in Figure 3.8 (b), the loss due to SPP modes decreases significantly with increasing ETL thickness. But meanwhile, it should be noted that the contribution of waveguide mode increases notably with thicker ETL. Therefore, the device does not necessarily gain extra outcoupled photons when placing emitter dipoles far away from the cathode. Quantitative calculations reveal that in planar OLED stacks typically around 50% of the light is trapped in waveguide and SPP modes.^[83,84,87,88]

4. Materials and Methods

4.1. Materials

All chemicals were used as received if not stated otherwise. All substrates were cleaned and put into the UV Ozone reactor for 20 min in the cleanroom (ISO 6) before coating the HIL/HTL.

Chemicals: Toluene, Acetone, ethanol, isopropanol, cyclohexane, 2,2'-Azobis(2-methylbutyronitrile), 1H,1H,2H,2H-Perfluorodecylacrylate, styrene, pentafluorophenyl acrylate, sodium dodecyl sulfate, perfluorohexane, perfluorooctanesulfonic acid (40 wt.% in H₂O), super yellow poly(*p*-phenylene vinylene) were purchased from *Sigma Aldrich*, poly(3,4-ethylenedioxythiophene):poly(styrene sulfonate) (Clevios Al 4083, 1.5 wt.%) was purchased from *Heraeus*, polystyrene latex (30 nm, 10 wt.%) was purchased from *Thermo Fisher*. Dry chlorobenzene was obtained from a *MBraun SPS 5 solvent purification system* in a nitrogen-filled glove box.

Substrates: Si substrates with native oxide layer, *BF33* glass substrates, Indium tin oxide (ITO) coated glass substrates.

4.2. Synthesis of polymeric nanoparticles dispersion

Sodium dodecyl sulfate (SDS)-stock solution was prepared by dissolving 40 mg SDS in 6 g deionized water. 500 mg monomer, 20 mg initiator were added in a 10 mL flask and stirred at 500 rpm for 5 min. 3 mL of the SDS-stock solution was added as continuous phase in the flask. The solution was kept stirring for one hour for pre-emulsification. The mini-emulsion was prepared by subsequently sonicating the mixture for 2 min at 90% amplitude under ice cooling using a *Branson sonifier W450* equipped with a 1/2" tip. The sample was stirred overnight at 72 °C in a silicon bath for 24 h. The dispersion was passed through a 1 µm PTFE syringe filter. The dispersion was concentrated by centrifugation (*Sigma 3-30KS*) at 7500 g for 20 min by using a centrifugal filter (*Amicon Ultra-3K, Merck*). The sample was redispersed in the filter with deionized water and

centrifuged again at 7500 g for 30 min to remove the excess surfactant SDS. This step was repeated until there was no predominant foam. Finally, the sample was recovered by centrifugation at 1000 g for 20 min and subsequently filtrated through a 0.45 μm PTFE syringe filter. It should be noted that the recipe and the amplitude of the sonication can be tuned to obtain different size nanoparticles.

4.3. Si substrate cleaning

Si substrates were loaded into a holder. The substrates were then submerged in a beaker with acetone in the ultrasonic bath for 5 min. Subsequently, the substrates were submerged in a beaker with propanol in the ultrasonic bath for 5 min. Finally, the substrates were blow dried with nitrogen and put in the oven at 140 °C for 10 min.

4.4. Glass/ITO substrates cleaning

Glass/ITO substrates were loaded into a holder and rinsed under the warm deionized water shower for 1-2 min. The plates were scrubbed with warm deionized water and neutral soap for 6 min. The substrates were rinsed again briefly under the warm deionized water shower and submerged in the warm deionized water bath for 7 min. Then, the substrates were sequentially submerged in a beaker with acetone and with propanol in ultrasonic bath for 5 min. Finally, they were dried with nitrogen and subsequently put in the oven at 140 °C for 10 min.

4.5. Preparation of Porous PEDOT:PSS layer

The PEDOT:PSS was used to form porous skeleton structure, while the polystyrene (PS) nanoparticles were used as porogen to control the porosity. First, 5 drops of 1% SDS aqueous solution was added to PEDOT:PSS dispersion and stirred to form homogeneous mixture. Calculated amount of PS latex was then added dropwisely, and kept stirring for a further 30 min to sufficiently mix the dispersions. The blends were spin-coated on the selected

substrate through a syringe mounted with a 0.45 μm filter head. An annealing process was done at 100 $^{\circ}\text{C}$ for 20 min in ambient atmosphere. As coated substrates were immersed in Toluene at room temperature or in cyclohexane at 70 $^{\circ}\text{C}$ for 5 min to remove post-added SDS and PS particles. Finally, the samples were dried with nitrogen.

4.6. Preparation of SYPPV solution

SYPPV was dissolved in dry chlorobenzene at a concentration of 6.5 g/mL, which was used for the spin coating as a light-emission layer. First, 26 mg SYPPV was added in a 20 mL glass vial. The glass vial was transferred into a glove box filled with nitrogen, in which 4 mL dry chlorobenzene was added to the glass vial. The sample was stirred overnight at 60 $^{\circ}\text{C}$ to form a homogeneous solution in the glove box.

4.7. OLEDs fabrication

A porous PEDOT:PSS layer was prepared on the ITO substrate. For a reference device, a 40 nm layer of PEDOT:PSS was filtered through a 0.45 μm PTFE filter head, then spin coated on the ITO substrate and subsequently annealed at 140 $^{\circ}\text{C}$ for 10 min in ambient atmosphere. The substrates were then transferred into a nitrogen-filled glove box, where SYPPV was spin coated on the PEDOT:PSS layer. Subsequently, the substrates were transferred into the evaporation chamber with a base pressure of $4\text{-}6\times 10^{-7}$ mbar, in which a Ba/Al (5 nm/ 100 nm) cathode was thermally evaporated. The Ba and Al layer were thermally deposited at a rate of 0.3 $\text{\AA}/\text{s}$ and 3 $\text{\AA}/\text{s}$, respectively. Deposition rates were monitored during material evaporation via quartz crystals. The device structure is demonstrated in Figure.

4.8. Dynamic light scattering (DLS) measurement

DLS measurements were performed with a commercial DLS device (*Zetasizer Nano ZS, Malvern Instruments*). Glass cuvettes were filled with 200 μL of sample and mounted into the DLS device. The average diameter of gyration of

the solute particles was calculated using the software of the DLS device.

4.9. Thermogravimetric analysis (TGA)

TGA was conducted on a thermogravimetric analyser from *METTLER TOLEDO*. The measurements were run from 25 °C to 900 °C with a heating rate 10 °C/min. The analysis of thermogravimetric data was performed using the software STAR^e SW 16.00.

4.10. Surface tension measurement

Surface tension was measured with a *Dataphysics DCAT 21 tensionmeter* employing the DuNoüy-Ring method.

4.11. Refractive index measurement

Refractive index was determined by ellipsometry with a *J.A. Woollam Alpha-SE Ellipsometer*. Ellipsometry is a non-destructive optical technique in which the sample to be characterized is illuminated with a beam of polarized light, as shown in Figure. Ellipsometry measures the change in polarization of light as a function of incident angle and wavelength, as shown in Figure 4.1. The experimentally determined ellipsometric values are Psi (Ψ) and Delta (Δ), which are related to the ration of Fresnel reflection coefficients R_p and R_s for p- and s- polarized light, respectively, by $\tan(\Psi) e^{i\Delta}$. Optical constants of the materials were then determined by first constructing an optical model of the sample with physically meaningful structural and optical parameters, and then by iteratively adjusting these parameters to obtain the best fit to the measured ellipsometric data, i.e., the fitting with the minimum mean square error (MSE). All the films for the refractive index measurement were coated on the Si substrates with native oxide layer. Since the Si substrate have better local surface roughness and overall bulk flatness, high refractive index (ca. 3.8 at 630 nm, which shows a big difference with the films and a better reflectivity) and absence of secondary back reflection, Si substrate is considered as a better substrate for ellipsometry within the vis-NIR region. Ellipsometry

measurements were performed over the wavelength range of 380 nm – 880 nm. The angles of light incidence were operated between 65° and 75° relative to the surface normal in steps of 5° for reflection ellipsometry. The analysis of the ellipsometric data was performed using the software *CompleteEASE* (J.A. Woollam Co.). A Tauc-Lorentz oscillator was used to fit the optical constants of PEDOT:PSS.

1. linearly polarized light ...

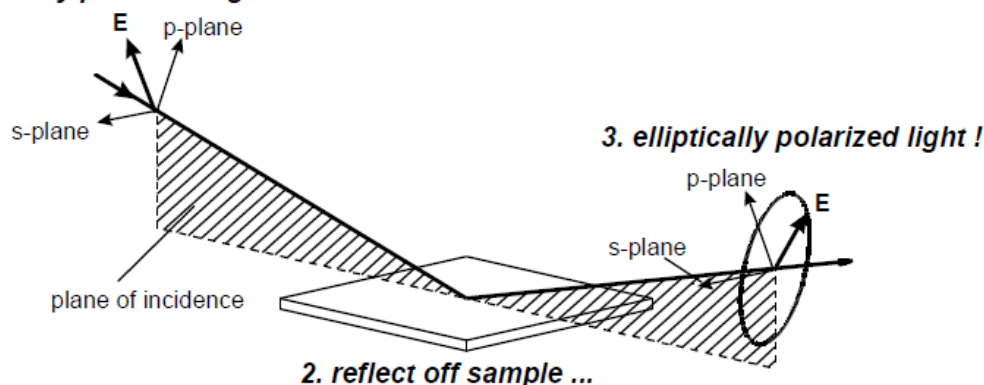


Figure 4.1.^[89] Interaction of polarized light with a sample.

Surface roughness was taken into account for the films consisted of fluorinated polymeric nanoparticles. Optically, roughness is like a lower-index surface film, as the roughness is a mixture of base material and air ($n=1$, $k=0$). *CompleteEASE* models this “layer” using the Bruggeman Effective Medium Approximation (EMA). Surface roughness in *CompleteEASE* is a mixed layer assuming 50% void content and 50% base material. A schematic of a sample with surface roughness is shown in Figure 4.2. It should be noted that this approximation to the actual sample works extremely well when the size of the surface roughness is much less than the wavelength of light used to measure the sample, which implies that the surface roughness features must be less than ~40 nm.

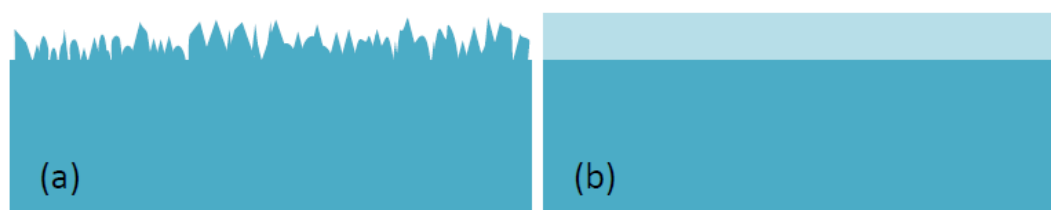


Figure 4.2.^[89] Schematic of (a) physical surface roughness; (b) optical model of surface roughness.

4.12. Transmission measurement

All films for the transmission measurement were coated on a bare *BF33* glass substrate. Transmission spectra were measured with a *Lambda 900 UVNIS/NIR* spectrometer. Transmitted light with a pathway perpendicular to the substrate was measured by the spectrometer. The transmission of a bare glass substrate was measured and used as a baseline measurement. Then the transmission of a substrate with the film coated on it was measured and compared to the bare substrate baseline to yield the percentage of light transmitted through the film without the inclusion of substrate reflection.

4.13. Atomic force microscopy (AFM) measurement

AFM measurements were done to characterize the morphology of thin films using a *Bruker Dimension ICON FastScan* atomic force microscope in the tapping mode in air with the scanning resolution of 512×512 pixel. A *VTESPA-300* tip was applied in the measurement.

4.14. Thickness measurement

The thickness of the film was measured with a *Bruker* profilometer. The film was scratched to form steps on the surface. The thickness measurement was carried out for each sample three times, and the thickness was then determined as the average.

4.15. Current density-voltage-luminescence measurement

The current density-voltage characterization was carried out with a *Keithley 2400* source unit, while the light output was measured simultaneously using a photodiode, connected to a *Keithley 6514* electrometer with the photodetector having an area larger than the emissive pixel, placed in close proximity to the emitting surface in order to capture all light emitted in the forward hemisphere. The substrate edges of the OLEDs were sealed by the sample holder to avoid detection of the waveguided light from the substrate mode.

4.16. Electroluminescence measurement

The electroluminescence spectra were recorded using an *Ocean Optics USB4000* spectrometer at different driving voltages.

5. Results and Discussion

5.1. Modification of PEDOT:PSS layer

5.1.1. Blending with fluorinated polymeric nanoparticles

Nanoparticles (NPs) have been widely used in optoelectronic devices including organic light-emitting diodes (OLEDs) to optimize their performances.^[90,91] As fluorinated polymers are one of the well-known materials possessing a very low refractive index, especially with a high degree of fluorination (i.e., refractive indices of 1.35-1.37),^[92–96] we proposed to lower the refractive index of PEDOT:PSS layer by embedding the fluorinated polymeric nanoparticles into the layer. For this purpose, NPs of poly(pentafluorophenyl acrylate) and poly(1H,1H,2H,2H-perfluorodecyl acrylate) were synthesized via mini-emulsion polymerization. Mini-emulsions were formulated by monomer, initiator, surfactant, co-stabilizer and deionized water, and the resulting polymer particles were characterized by dynamic light scattering after dilution, as shown in Table 5.1. The corresponding chemical structure are shown in Figure 5.1.

Table 5.1. Synthesis of fluorinated polymer nanoparticles via mini-emulsion polymerization^a

code	monomer (mg)		initiator (mg)	surfactant (mg)		Deionized water (g)	diameter (nm)
	PFPA	4H-PFDA	V59	SDS	PFOS		
NP1	500	-	30	20	-	3	217
NP2	500	-	30	60	-	3	180
NP3	500		30	-	70	3	60
NP4	-	500	30	20	-	3	140
NP5	-	500	30	50	-	3	92

^aFor the monomer, PFPA and 4H-PFDA represent pentafluorophenyl acrylate and 1H,1H,2H,2H-perfluorodecyl acrylate, respectively. V59, i.e., 2,2'-Azobis(2-methylbutyronitrile), is an oil-soluble azo polymerization initiator. For the surfactant, SDS and PFOS represent sodium dodecyl sulfate and perfluorooctanesulfonic acid, respectively. It is noted that 30 mg of perfluorohexane was also added as the co-stabilizer in each case

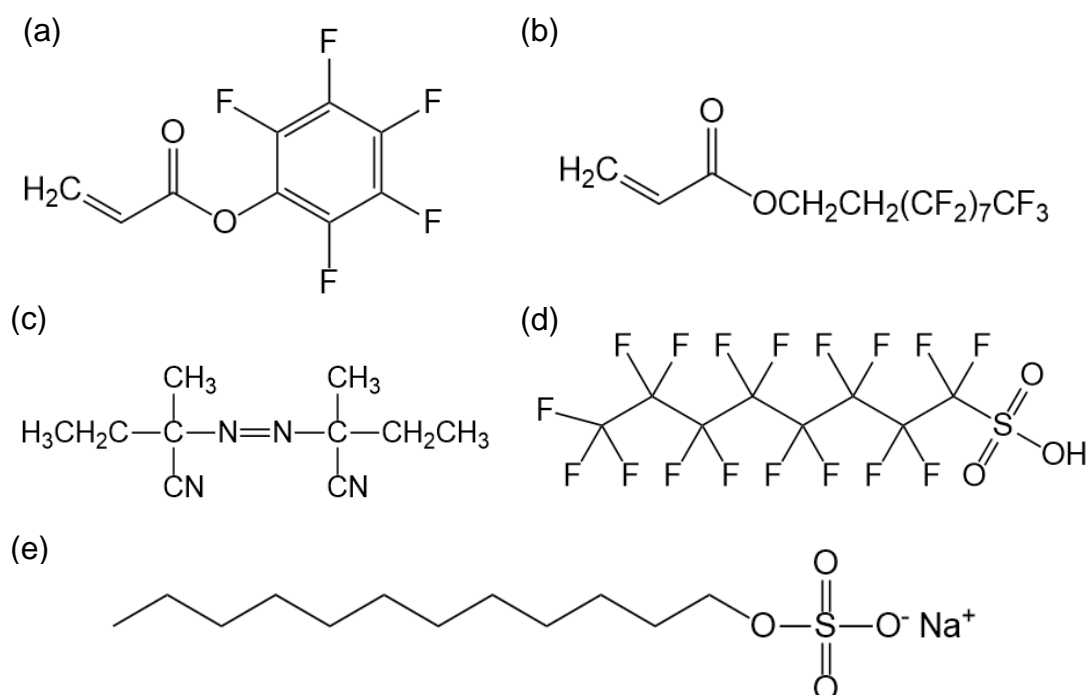


Figure 5.1. Chemical structure of (a) PFPA (pentafluorophenyl acrylate), (b) 4H-PFDA (1H,1H,2H,2H-perfluorodecyl acrylate), (c) V59 (2,2'-Azobis(2-methylbutyronitrile)), (d) PFOS (perfluorooctanesulfonic acid) and (e) SDS (sodium dodecyl sulfate).

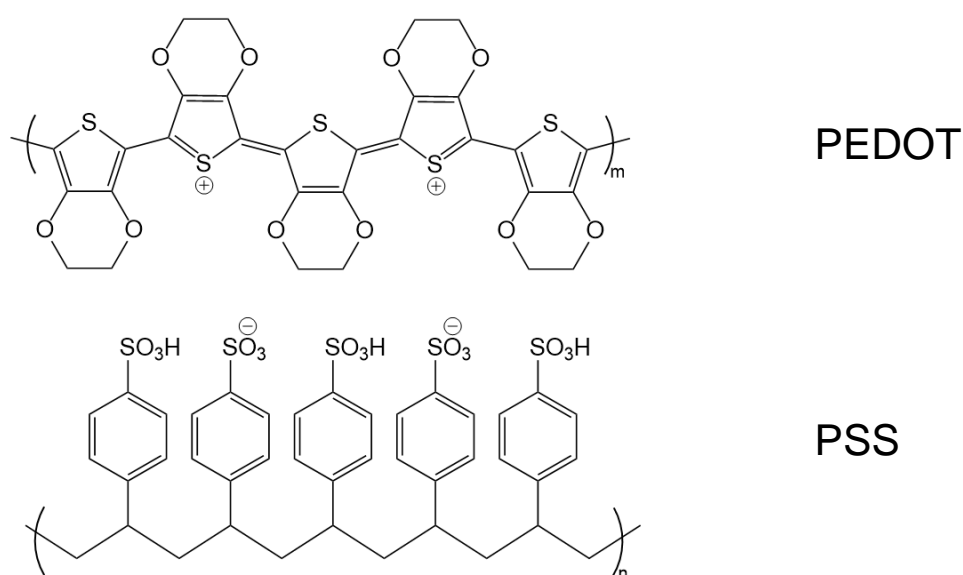


Figure 5.2. Chemical structure of PEDOT:PSS.

By comparing NP1/NP4 with NP2/NP5, it is found that smaller size of the resulting polymeric NPs can be obtained with a higher surfactant-to-monomer concentration. This is mainly because higher surfactant concentration result in a higher surface coverage which is required to stabilize smaller droplets.^[97,98]

In the case of NP3, 60 nm of particle size was reached by employing fluorinated surfactant, as fluorinated surfactants are highly surface active and much more efficient than the hydrocarbon ones.^[99,100] While the thickness of PEDOT:PSS layer in the OLED devices is around 40 nm, small-sized nanoparticles are more preferred. If the nanoparticles are too big, it will disrupt the structure of OLED devices and may cause defects. Hence, only NP3 and NP5 were considered to blend with PEDOT:PSS (chemical structure shown in) dispersion (1.5 wt.%, Al4083). A uniform film formation would require removing as much surfactant as possible. Otherwise, removal too much surfactant destabilizes the nanoparticle dispersion and compromises its processability due to a rise in surface tension.^[101] Therefore, we removed the excess surfactant by redispersing the nanoparticle dispersion with additional deionized water in a centrifugal filter and subsequently under centrifugation. Finally, the sample NP3 and NP5 were concentrated by centrifugation to 6 wt.% and 10 wt.% solid contents, respectively. To fabricate the nanoparticle embedded PEDOT:PSS layers, each nanoparticle dispersion was re-dispersed into PEDOT:PSS dispersion with a weight ratio of 1:1 and the mixture was simply spin-coated onto Si or ITO coated glass substrates. However, flocculation emerged in the blend of NP3 and PEDOT:PSS and the film spin-coated after 0.45 μm syringe filtration on Si substrates showing large-scale defects, as shown in Figure 5.3 (a). To figure out the reason behind this phenomenon, we added only one drop of PFOS (40 wt.% in water) into 2 mL PEDOT:PSS dispersion and observed the flocculation as well, indicating PFOS could destabilize PEDOT:PSS dispersion. On the other hand, the surface tension of the PEDOT:PSS dispersion and NP3-(PEDOT:PSS) blend were 56 mN/m and 26 mN/m, respectively. In relation to this, Ribeiro *et al.* found a surface tension of the dispersion of around 60 mN/m to be an ideal compromise between stability and good wetting behavior.^[101] From these aspects, the mainly reason for the non-uniform NP3-PEDOT:PSS blend film could be the very low surface tension (dewetting effect) and destabilization of the blend dispersion caused by PFOS. In the case of the NP5-PEDOT:PSS blend, it exhibited a reproducible uniform film on Si substrate. It should be noted that using a concentrated NP dispersion for the blend exhibited improved film formation compared with dilute NP dispersions, which is in agreement with observations by Colberts *et al.*^[102]

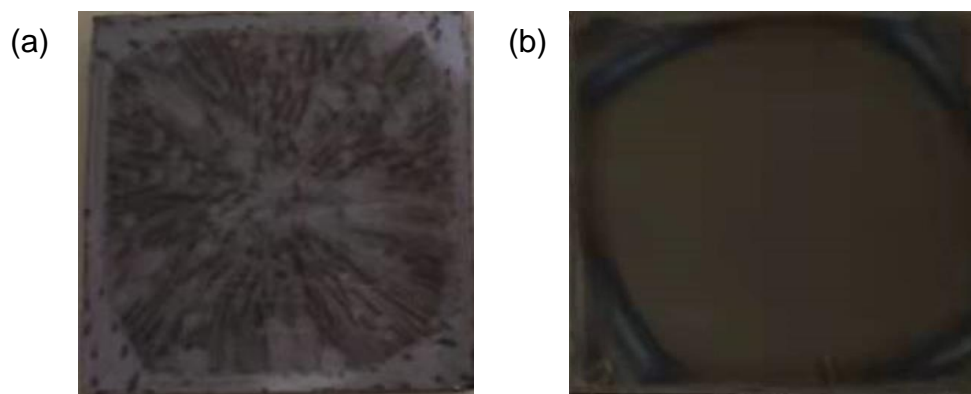


Figure 5.3. (a) NP3-PEDOT:PSS blend film spin-coated on Si substrate. (b) NP5-PEDOT:PSS blend film spin-coated on Si substrate.

Variable angle spectroscopic ellipsometry (VASE) was used to measure the refractive indices of the films, the fits and the resulting refractive indices of PEDOT:PSS and NP5-PEDOT:PSS films are shown in Appendix and Figure 5.4., respectively. The thicknesses of PEDOT:PSS and NP5-PEDOT:PSS films were 43 nm and 47 nm (measured by profilometry), respectively. Due to the thin thickness (~ 40 nm) of PEDOT:PSS, optical anisotropy is indistinguishable in such a thin film so that an isotropic model could well fit the ellipsometric results, as shown in Appendix. As we can see from Figure 5.4, the refractive index can be lowered from 1.54 to 1.42 at 550 nm by introducing NP5 into PEDOT:PSS layer. The difference is around 0.13 in the whole visible wavelength region. It should be noted that the reduction of the refractive index is strongly limited by the refractive index of NP5 (~ 1.35).

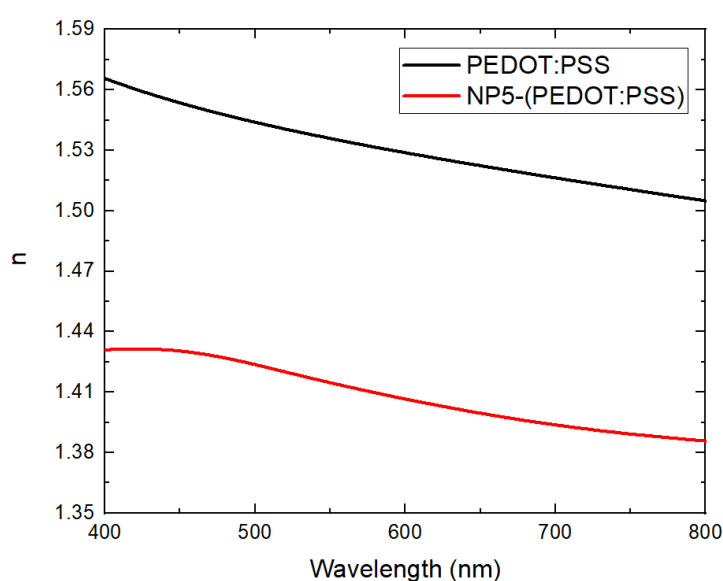


Figure 5.4. Refractive indices (n) spectra of PEDOT:PSS and NP5-PEDOT:PSS thin films.

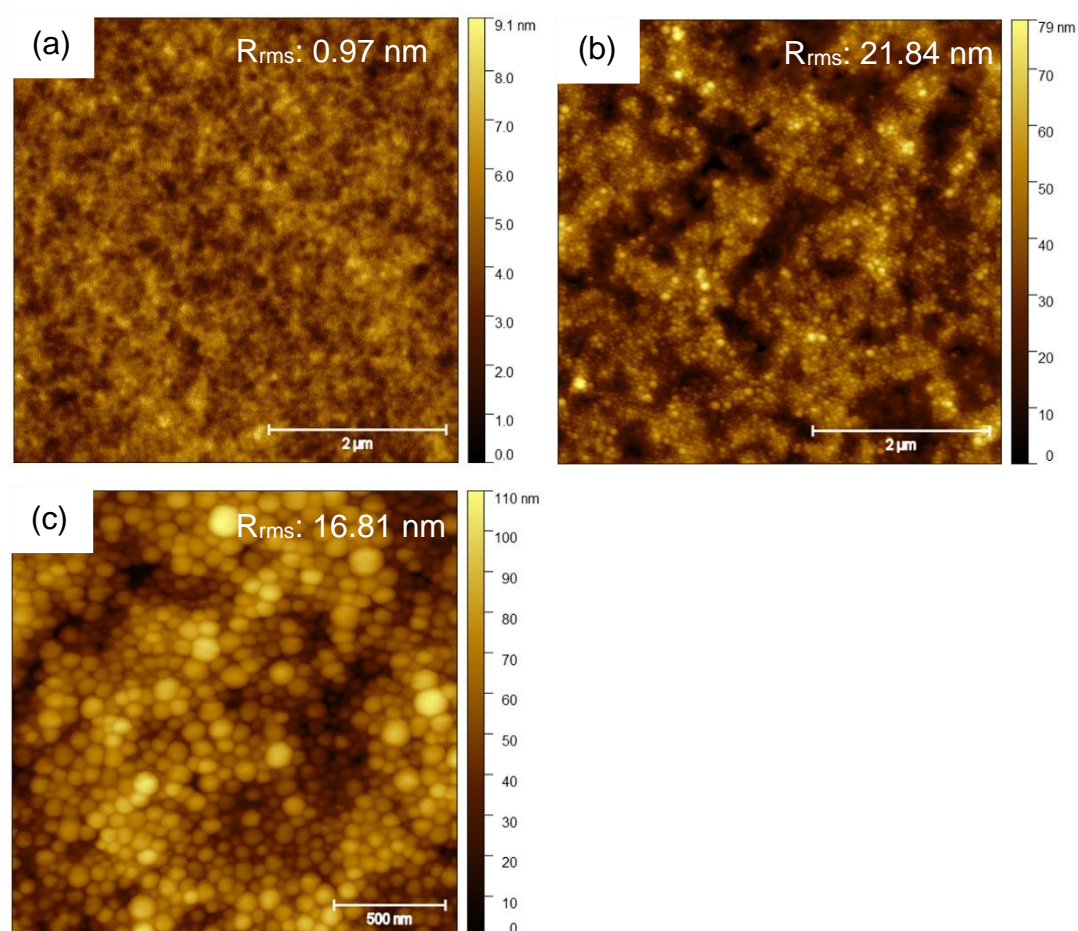


Figure 5.5. AFM images of (a) PEDOT:PSS film with scale 5×5 μm, (b) and (c) NP5-(PEDOT:PSS) film with scale 5×5 μm and 2×2 μm, respectively. The surface roughness (R_{rms}) value is indicated in the AFM images.

The atomic force microscope (AFM) topography images of PEDOT:PSS and NP5-PEDOT:PSS are shown in Figure 5.5. In contrast to the flat surface of PEDOT:PSS thin film, the NP5-PEDOT:PSS layer exhibits a large amount of nanoparticles distributed in the film without remarkable agglomeration. The diameters of the nanoparticles are mainly in the range 70-120 nm, which is consistent with DLS measurements. Due to the large size of nanoparticles, the root-mean-square (RMS) roughness value of NP5-PEDOT:PSS film is 21.84 nm, whereas the PEDOT:PSS thin film shows a very smooth surface with a RMS roughness of 0.97 nm. It is expected that the higher roughness of nanoparticle-embedded PEDOT:PSS layer would not cause electrical short in OLED devices as reported by several studies.^[91,103,104]

5.1.2. Formation of porous structure

Another approach to lower the refractive index of a material is the formation of porous structure, i.e., introducing voids into the material. For this purpose, polystyrene (PS) nanoparticles were used in this work as sacrificial material to yield porous structure, as Jiang *et al.* reported for blends of PS and PMMA nanoparticles.^[105] 30 nm averaged size PS latex particles dispersed in deionized water with the concentration 10 wt.% were purchased from Thermo Fischer. In addition, 100 nm averaged size PS latex particles stabilized by SDS were synthesized and dispersed in deionized water with the concentration 10 wt.%. In order to construct a porous structure, we blended PS dispersion with PEDOT:PSS dispersion, spin-coated the blends on the substrates and subsequently submerged the films into toluene to remove the PS particles.

We have prepared three blends for the investigation, i.e., the blend of 30 nm PS NP dispersion and PEDOT:PSS with a weight ratio 1:1, the blend of 100 nm PS NP dispersion and PEDOT:PSS with a weight ratio 1:1 and the blend of 100 nm PS NP dispersion and PEDOT:PSS with a weight ratio 1:3. These blends are denominated as PS(30nm)-PEDOT:PSS (1:1), PS(100nm)-PEDOT:PSS (1:1) and PS(100nm)-PEDOT:PSS (1:3), respectively. However, we found that 30 nm PS nanoparticles were hardly removed after immersion into toluene, as shown in Figure 5.6 (a) and (b). This is mainly because the small sized PS NPs were buried in the film so that toluene was not able to reach the NPs and dissolve them. On the contrary, porosity was observed in the films generated from the blends with 100 nm PS NPs, as shown in Figure 5.7 (c)-(f). The porosity can be tuned by the fraction of PS NPs. With higher fraction of PS NPs, more voids can be found in the film, as compared Figure 5.7 (c) with Figure 5.7 (e). Due to the intrinsic porosity, the RMS roughness values of PS(100nm)-PEDOT:PSS (1:1) and PS(100nm)-PEDOT:PSS (1:3) films are much higher than PEDOT:PSS films, i.e., 22.05 nm and 19.36 nm, respectively.

Due to the porosity, the refractive indices of the layer prepared from blends with 100 nm PS NPs are expected to be significantly lower in comparison to the compact PEDOT:PSS thin film. The refractive indices were determined by VASE, and the data were fit using an effective medium approximation (EMA model), which is able to predict the effective refractive index of multicomponent

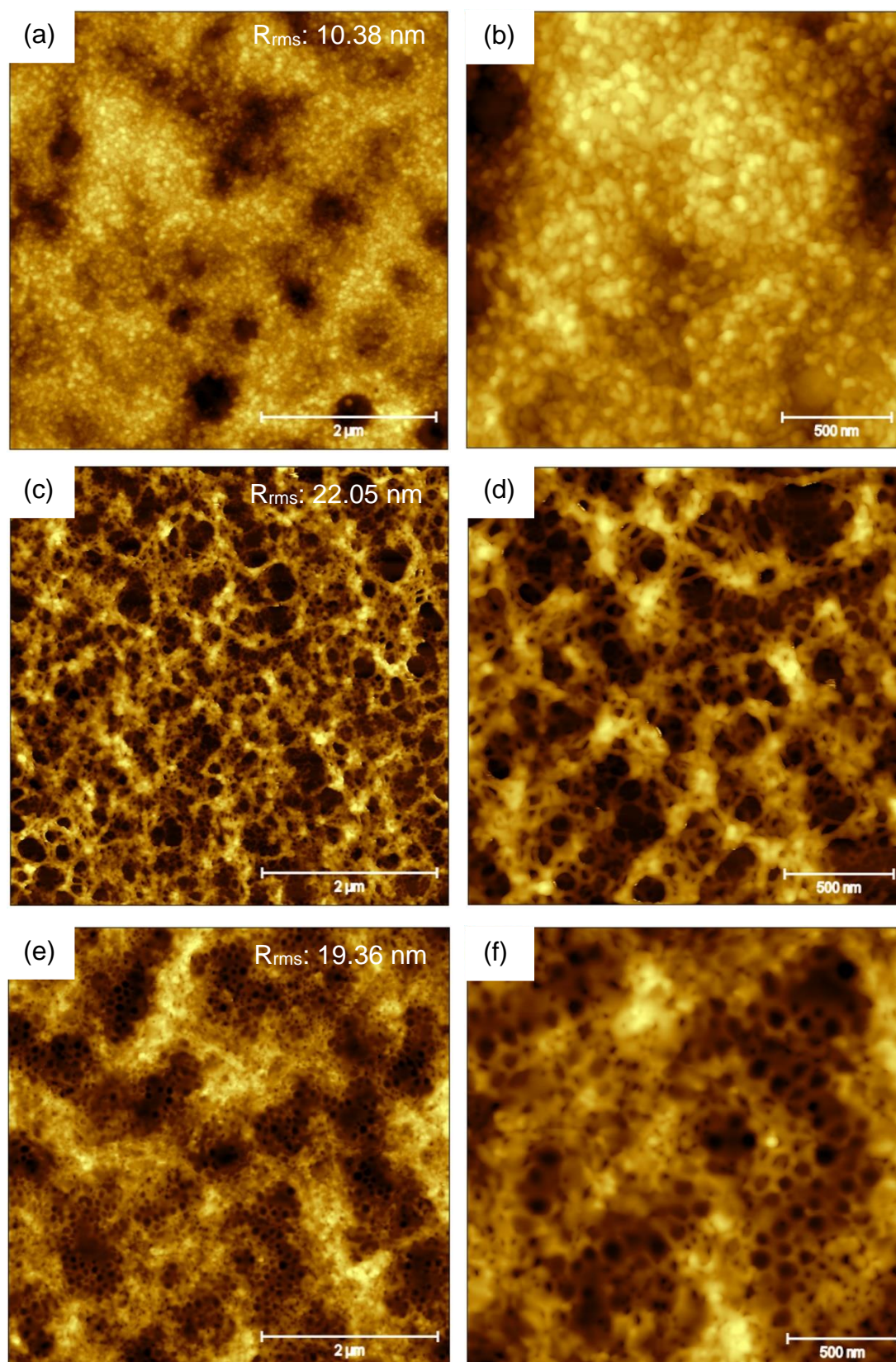


Figure 5.6. AFM images of (a) and (b) PS(30 nm)-PEDOT:PSS with a weight ratio 1:1 in the scale of scale $5 \times 5 \mu\text{m}$ and $2 \times 2 \mu\text{m}$, respectively. (c) and (d) PS(100 nm)-PEDOT:PSS with a weight ratio 1:1 in the scale of scale $5 \times 5 \mu\text{m}$ and $2 \times 2 \mu\text{m}$, respectively. (e) and (f) PS(100 nm)-PEDOT:PSS with a weight ratio 1:3 in the scale of scale $5 \times 5 \mu\text{m}$ and $2 \times 2 \mu\text{m}$, respectively. The R_{rms} is indicated in the AFM images.

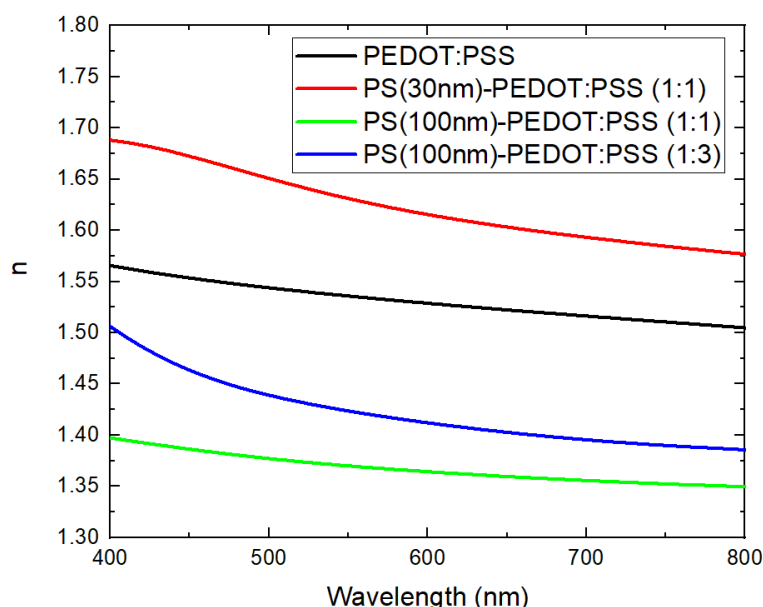


Figure 5.7. Refractive indices (n) spectra of PEDOT:PSS, the blends PS(30nm)-PEDOT:PSS (1:1), PS(100nm)-PEDOT:PSS (1:1) and PS(100nm)-PEDOT:PSS (1:3) thin films.

material (in this case PEDOT:PSS and voids). The fits are shown in Appendix and the resulting refractive index spectra are shown in Figure 5.7. The refractive index of PS(30 nm)-PEDOT:PSS (1:1) is ~ 0.2 higher than the PEDOT:PSS, indicating a large amount of PS NPs were not removed, which was also proven by the AFM topography images. As expected, the refractive indices of porous PEDOT:PSS films are reduced, and lower with a larger fraction of 100 nm PS NPs. The blend PS(100nm)-PEDOT:PSS with a weight ratio 1:1 and 1:3 have decreased the refractive index of PEDOT:PSS layer from 1.54 to 1.36 and 1.42 at 550 nm, respectively.

In addition, we investigated the transmittance of the PEDOT:PSS film and the porous films generated from the blends of 100 nm PS NPs and PEDOT:PSS with a weight ratio 1:1 and 1:3. The films were coated on cleaned glass substrates. The thickness of each film was 43 nm, 41 nm and 55 nm, respectively. Before measuring the transmittance of the films, a cleaned bare glass substrate was set as baseline and the results are presented in Figure 5.8. Although the PEDOT:PSS thin film already shows a relative high transmittance, 95-97% in the visible wavelength region, almost unity optical transmittance was reached for our porous PEDOT:PSS thin films.

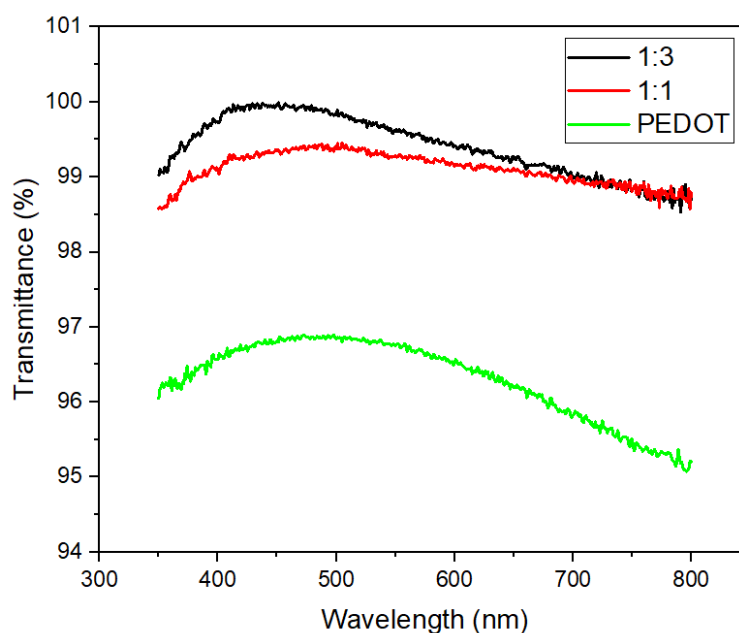


Figure 5.8. Transmittance spectra of PEDOT:PSS layer and the porous PEDOT:PSS layers generated from the blends PS(100nm)-PEDOT:PSS with a weight ratio 1:1 and 1:3.

5.2. OLEDs integrated with modified PEDOT:PSS layers

For the OLEDs studied in this work, we used super yellow poly(p-phenylene vinylene) (SYPPV) as emissive material. To fabricate the OLEDs, HTLs (PEDOT:PSS and modified PEDOT:PSS layers) were prepared onto ITO coated glass substrates by spin-coating process and immersion into toluene (for the case of porous PEDOT:PSS layer), SYPPV was then spin-coated onto the HTLs as EML, in the end a Ba/Al cathode was applied onto the EML by vapor deposition. It should be noted that the thickness of all HTLs were tuned to be 40~50 nm by adjusting the spin speed. In order to obtain optoelectrical characterization and performance of the OLED devices, the devices were subjected to voltage sweeps during which the current flowing through the devices and the photocurrent as well as electroluminescence spectra were recorded.

Figure 5.9 (a) shows the current density-voltage-luminance (J - V - L) characteristics of the OLED devices integrated with pristine PEDOT:PSS (reference device), NP5-PEDOT:PSS (1:1) (i.e., nanoparticle-embedded

PEDOT:PSS), and PS(100nm)-PEDOT:PSS (1:1) (i.e., porous PEDOT:PSS) layers. For $|V| < 2\text{ V}$ all devices exhibit low leakage current. Besides the OLEDs integrated with modified PEDOT:PSS layers have the similar turn-on voltage compared to the reference device and current increases at $V \approx 2\text{ V}$ exponentially similar to the reference device indicating that fully efficient charge injection and transport. These results confirmed that the modifications of PEDOT:PSS layer either by embedding nanoparticles or introducing voids have no negative effect on the hole injection and transport. Furthermore, no current hysteresis was observed in all OLED devices.

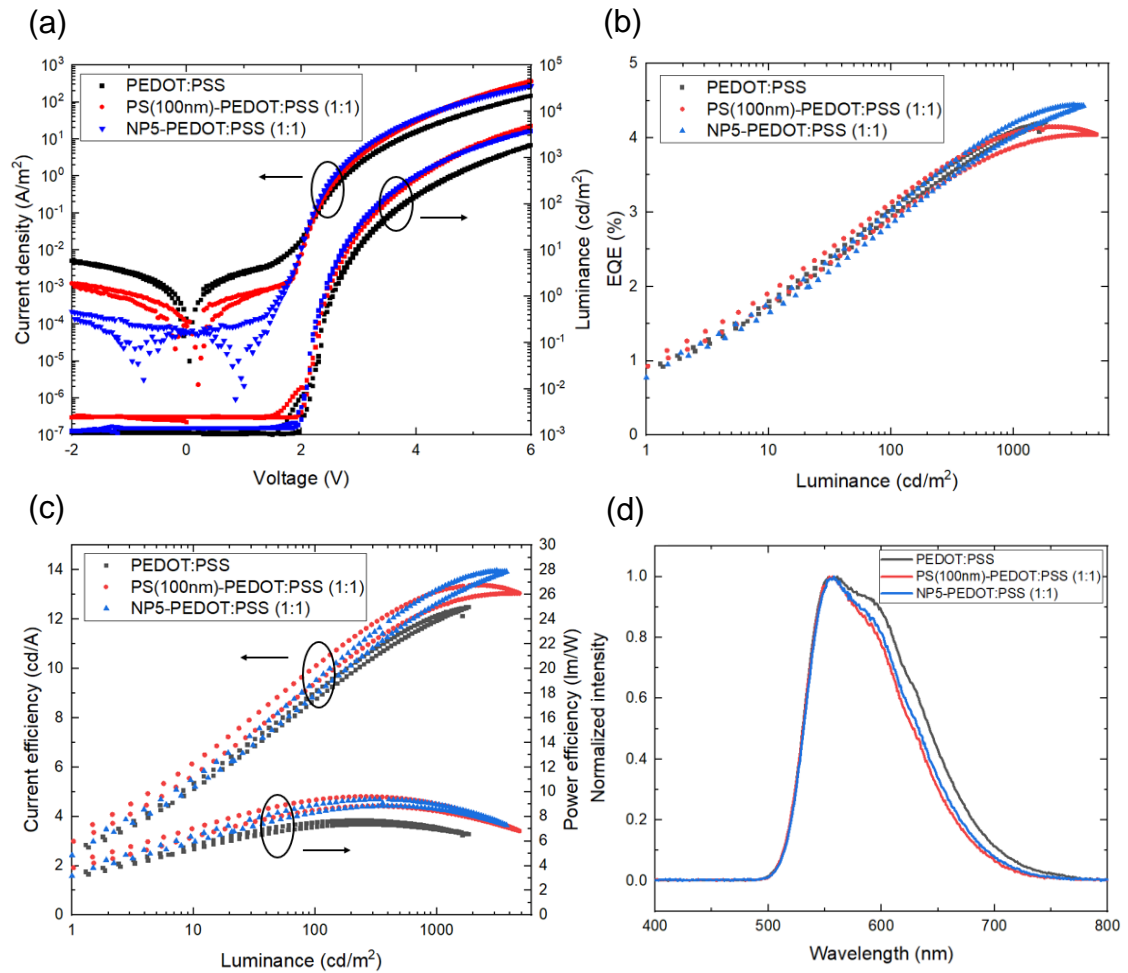


Figure 5.9. Device performance of OLEDs with different HTLs dominated as PEDOT:PSS, PS(100nm)-PEDOT:PSS (1:1) and NP5-PEDOT:PSS (1:1). (a) Current density-voltage-luminance (J-V-L) characteristics. (b) External quantum efficiency versus luminance. (c) Current efficiency and power efficiency versus luminance. (d) Electroluminescence spectra.

The plot of EQE versus luminance is shown in Figure 5.9 (b). All devices show

the similar EQE at luminances in the range of 1-1000 cd/m^2 . To gain a deeper understanding of this result, an optical simulation of the outcoupling efficiency for our OLED stack (Figure 5.10 (a)) was performed. The numerical simulation of position-dependent outcoupling efficiency to air modes $\eta_A(x)$ with the refractive index of PEDOT:PSS layer ranging from 1.8 to 1.0 in the SYPPV OLEDs is shown in Figure 5.10. It is shown that reducing the refractive index of PEDOT:PSS from 1.6 to 1.4 can achieve an increase in the outcoupling efficiency of 5% when emitting dipoles are located at the position with a distance of 60 nm away from the metallic cathode. As mentioned in the former section, the refractive indices of pristine PEDOT:PSS, NP5-PEDOT:PSS (1:1) and PS(100nm)-PEDOT:PSS (1:1) layers are 1.54, 1.41 and 1.36 at 550 nm, respectively. Therefore, about 3% enhancement of EQE is expected for the OLEDs integrated modified PEDOT:PSS layers which is hard to be observed experimentally (likely within the experimental error).

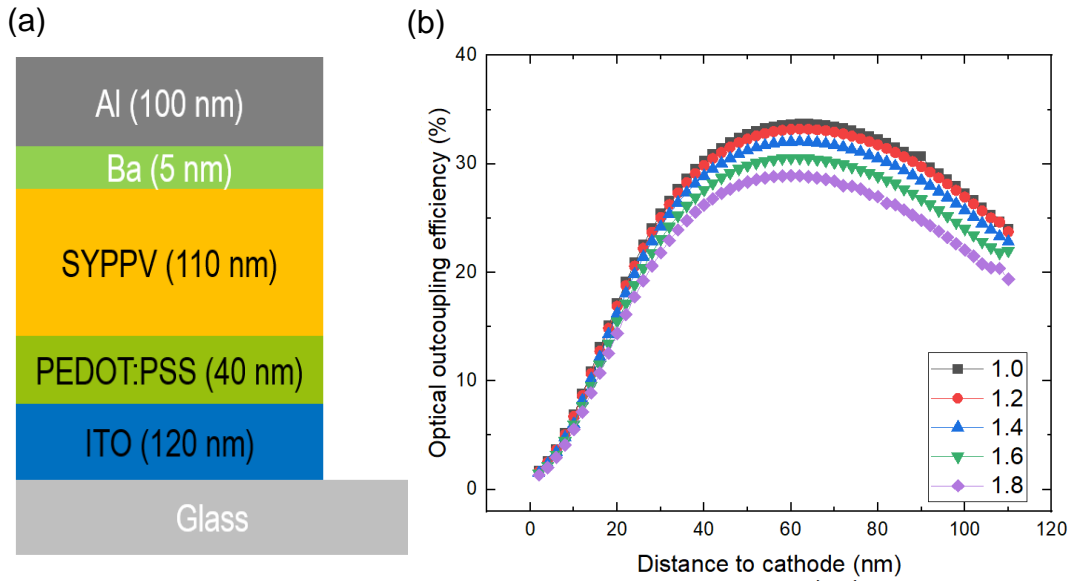


Figure 5.10. (a) OLED structure for the simulation. (b) The position-dependent optical outcoupling efficiency with the refractive index of PEDOT:PSS layer ranging from 1.8 to 1.2. The anisotropic factor of SYPPV was 0.029. The simulation was performed by Dr. Yungui Li.

Figure 5.9 (c) shows current efficiency and power efficiency of the OLED devices as a function of luminance. For all devices, the current efficiency increases with higher luminance in the range of 1-1000 cd/m^2 . Both devices with modified HTL exhibit an improvement of current efficiency by a factor of 1.10 at luminance of 300 cd/m^2 and 1000 cd/m^2 . This improvement for the

devices with modified HTL is because of the changed electroluminescence (EL) spectrum (Figure 5.9 (d)), which is closer to the optimal luminosity curve. In contrast to the current efficiency, the maximum power efficiency can reach 9.6 lm/W for devices with modified HTL at luminance of 300 cd/m² and it slightly rolls off to 8.9 lm/W at 1000 cd/m². The power efficiency of reference device at luminance of 300 cd/m² and 1000 cd/m² are 7.6 lm/W and 7.1 lm/W, respectively. Compared with reference device, the devices with modified HTLs shows a 26% enhancement in the power efficiency. This enhancement is because the voltage is lower at the same current density, which may caused by the thinner effective layer thickness. For all devices, very similar electroluminescence (EL) spectrum is observed, with the peak at 550 nm, as shown in Figure 5.9 (d). A minor change in the EL spectra is observed in the devices with modified HTLs, which might result from the different optical cavity length.^[106] In addition, the thickness of organic layers (HTL+EML) in the OLED devices with PEDOT:PSS, NP5-PEDOT:PSS (1:1) and PS(100nm)-PEDOT:PSS (1:1) layers were measured by profilometry, and were 152 nm, 145 nm and 111 nm, respectively. Since all HTLs were controlled to be around 45 nm, we suspected that spin-coating EML on porous HTL would cause the collapse of the porous structure and the emissive molecules may also fill the voids. Therefore, to fabricate the remaining layers on top of such a porous HTL by thermal evaporation could be the best way to avoid the intermixing. In this way, intermixing is limited to the surface and most voids could be preserved. To achieve this, an inverted OLED structure would be a feasible choice, which would be discussed in the outlook of this thesis.

6. Conclusions and Outlook

This chapter summarizes the main results of this work and gives an outlook on the further investigations.

First of all, synthesis of fluorinated polymer nanoparticles via mini-emulsion polymerization was conducted in this work. The particle size can be tuned by the amount of surfactant. In order to obtain good film quality, the excess surfactant should be removed as much as possible. As of this aspect, we found although smaller nanoparticle size (diameter of 60 nm) can be formed using the fluorosurfactant PFOS, it hindered the formation of uniform films. This is mainly due to the dewetting effect caused by PFOS, as only a little amount of PFOS can significantly lower the surface tension of the dispersion due to its high surface activity.

Next, two different approaches are presented to lower the refractive index of PEDOT:PSS layer. The first approach is to form a fluorinated polymer nanoparticle-embedded PEDOT:PSS layer, which can be achieved by spin-coating the blend of PEDOT:PSS dispersion and fluorinated polymer nanoparticles dispersion on the substrates. The second approach is to construct a porous PEDOT:PSS layer, which can be achieved by spin-coating the blend of PEDOT:PSS dispersion and PS nanoparticles dispersion on the substrate and subsequently selectively remove the PS nanoparticles by immersion in toluene. By applying these two methods, the refractive index of PEDOT:PSS layer has been reduced from 1.54 to 1.41 and 1.37 at 550 nm, respectively. It is noteworthy that the refractive index can be tuned by the fraction of fluorinated polymer nanoparticles and PS nanoparticles.

Furthermore, we investigated the performance of OLEDs integrated with the modified PEDOT:PSS layer. The J - V - L characteristics exhibit low leakage current and turn-on voltage, which is similar to the reference device, indicating that these modifications on PEDOT:PSS layer have no negative impact on the

hole injection and transport. However, no obvious improvement in the external quantum efficiency was observed in the OLEDs integrated with modified PEDOT:PSS layers. This is mainly due to the small effect the refractive index of the HTL has on the outcoupling efficiency. When used in an inverted structure with the low- n transport layer between the emitting material and the metal, larger improvements are expected.

In addition, the thickness of the organic layers in the device with porous PEDOT:PSS layer was found much thinner than the other two devices. We suspected that the solution processed EML would cause the collapse of the porous structure and the emissive molecules would also fill the voids. To tackle this problem, an inverted OLED structure could be an option. Figure 6.1 shows an inverted OLED device architecture and the proposed energy levels of the OLED reported by Colsmann *et al.*,^[107] where PEDOT:PSS layer can be inserted between Al and MoO₃ or even replace the aluminum top-anode. As PEDOT:PSS is at the top of the organic layer or even the whole OLED stack, the porosity can be preserved. On the other hand, the effect of the solution, used for the removal of PS nanoparticles, on the other layers should be taken into account. Since toluene can dissolve SYPPV, cyclohexane could be the alternative solution to selectively remove PS nanoparticles.

Finally, these two approaches presented in this thesis, to reduce the refractive index of a material, are considered feasible to be applied also in other solution processed layers in the OLED, such as ETL and EML.

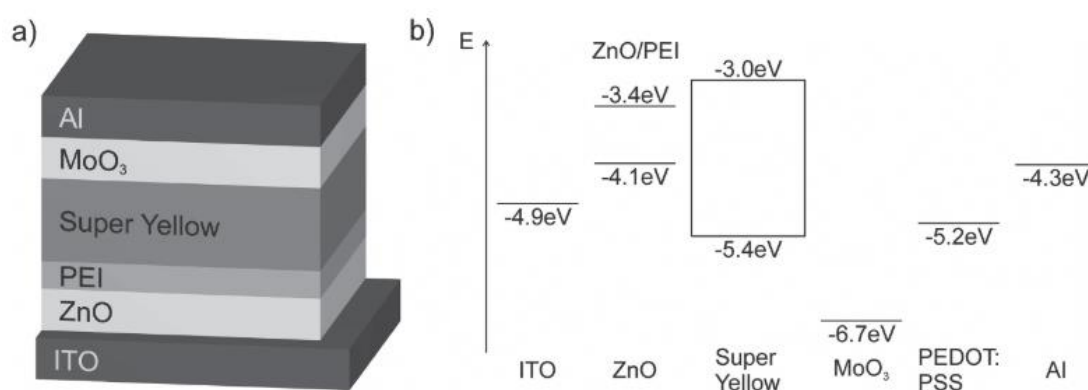


Figure 6.1.^[107] (a) Inverted OLED device structure. (b) Proposed energy levels of the OLED.

7. References

- [1] C. W. Tang, S. A. Vanslyke, *Appl. Phys. Lett.* **1987**, 51, 913.
- [2] M. A. Baldo, D. F. O'Brien, Y. You, A. Shoustikov, S. Sibley, M. E. Thompson, S. R. Forrest, *Nature* **1998**, 395, 151.
- [3] M. A. Baldo, S. Lamansky, P. E. Burrows, M. E. Thompson, S. R. Forrest, *Appl. Phys. Lett.* **1999**, 75, 4.
- [4] H. Uoyama, K. Goushi, K. Shizu, H. Nomura, C. Adachi, *Nature* **2012**, 492, 234.
- [5] K. Walzer, B. Maennig, M. Pfeiffer, K. Leo, *Chem. Rev.* **2007**, 107, 1233.
- [6] G. He, M. Pfeiffer, K. Leo, M. Hofmann, J. Birnstock, R. Pudzich, J. Salbeck, *Appl. Phys. Lett.* **2004**, 85, 3911.
- [7] H. Yang, Y. Zhao, J. Hou, S. Liu, *Microelectronics J.* **2006**, 37, 1271.
- [8] A. Salehi, Y. Chen, X. Fu, C. Peng, F. So, *ACS Appl. Mater. Interfaces* **2018**, 10, 9595.
- [9] T. C. Rosenow, M. Furno, S. Reineke, S. Olthof, B. Lüssem, K. Leo, *J. Appl. Phys.* **2010**, 108, 113113.
- [10] S. Reineke, F. Lindner, G. Schwartz, N. Seidler, K. Walzer, B. Lüssem, K. Leo, *Nature* **2009**, 459, 234.
- [11] S. Mladenovski, K. Neyts, D. Pavicic, A. Werner, C. Rothe, *Opt. Express* **2009**, 17, 7562.
- [12] H. Greiner, *Jpn. J. Appl. Phys.* **2007**, 46, 4125.
- [13] S. Reineke, M. Thomschke, B. Lüssem, K. Leo, *Rev. Mod. Phys.* **2013**, 85, 1245.
- [14] B. W. D'Andrade, J. J. Brown, *Appl. Phys. Lett.* **2006**, 88, 192908.
- [15] Y. Sun, S. R. Forrest, *J. Appl. Phys.* **2006**, 100, 73106.
- [16] J. P. Yang, Q. Y. Bao, Z. Q. Xu, Y. Q. Li, J. X. Tang, S. Shen, *Appl. Phys. Lett.* **2010**, 97, 256.

- [17] S.-H. Eom, E. Wrzesniewski, J. Xue, *Org. Electron.* **2011**, 12, 472.
- [18] J.-H. Lee, Y.-H. Ho, K.-Y. Chen, H.-Y. Lin, J.-H. Fang, S.-C. Hsu, J.-R. Lin, M.-K. Wei, *Opt. Express* **2008**, 16, 21184.
- [19] S. Möller, S. R. Forrest, *J. Appl. Phys.* **2002**, 91, 3324.
- [20] S.-I. Tanaka, Y. Kawakami, Y. Naito, in *Proc.SPIE*, **2004**.
- [21] C. F. Madigan, M.-H. Lu, J. C. Sturm, *Appl. Phys. Lett.* **2000**, 76, 1650.
- [22] T.-W. Koh, H. Cho, C. Yun, S. Yoo, *Org. Electron.* **2012**, 13, 3145.
- [23] T. W. Koh, J. A. Spechler, K. M. Lee, C. B. Arnold, B. P. Rand, *ACS Photonics* **2015**, 2, 1366.
- [24] S. Chen, H. S. Kwok, *Opt. Express* **2010**, 18, 37.
- [25] J. J. Shiang, T. J. Faircloth, A. R. Duggal, *J. Appl. Phys.* **2004**, 95, 2889.
- [26] W. H. Koo, S. M. Jeong, F. Araoka, K. Ishikawa, S. Nishimura, T. Toyooka, H. Takezoe, *Nat. Photonics* **2010**, 4, 222.
- [27] Y. Sun, S. R. Forrest, *Nat. Photonics* **2008**, 2, 483.
- [28] J. Feng, Y. F. Liu, Y. G. Bi, H. B. Sun, *Laser Photonics Rev.* **2017**, 11, DOI 10.1002/lpor.201600145.
- [29] G. Gomard, J. B. Preinfalk, A. Egel, U. Lemmer, *J. Photonics Energy* **2016**, 6, 030901.
- [30] C. Fuchs, T. Schwab, T. Roch, S. Eckardt, A. Lasagni, S. Hofmann, B. Lüssem, L. Müller-Meskamp, K. Leo, M. C. Gather, R. Scholz, *Opt. Express* **2013**, 21, 16319.
- [31] T. W. Koh, J. M. Choi, S. Lee, S. Yoo, *Adv. Mater.* **2010**, 22, 1849.
- [32] B. D. To, C.-C. Yu, J.-R. Ho, H.-C. Kan, C. C. Hsu, *Org. Electron.* **2018**, 53, 160.
- [33] L. Zhou, Q.-D. Ou, J.-D. Chen, S. Shen, J.-X. Tang, Y.-Q. Li, S.-T. Lee, *Sci. Rep.* **2014**, 4, 4040.
- [34] T. Schwab, C. Fuchs, R. Scholz, A. Zakhidov, K. Leo, M. C. Gather, *Opt. Express* **2014**, 22, 7524.

- [35] P.-A. Will, E. B. Schwarz, C. Fuchs, R. Scholz, S. Lenk, S. Reineke, *Org. Electron.* **2018**, *58*, 250.
- [36] A. Salehi, S. Ho, Y. Chen, C. Peng, H. Yersin, F. So, *Adv. Opt. Mater.* **2017**, *5*, 1700197.
- [37] H. Shin, J.-H. Lee, C.-K. Moon, J.-S. Huh, B. Sim, J.-J. Kim, *Adv. Mater.* **2016**, *28*, 4920.
- [38] A. Kumar, R. Srivastava, M. N. Kamalasanan, D. S. Mehta, *Opt. Lett.* **2012**, *37*, 575.
- [39] M. K. Callens, D. Yokoyama, K. Neyts, *Opt. Express* **2015**, *23*, 21128.
- [40] W. L. Barnes, *J. Mod. Opt.* **1998**, *45*, 661.
- [41] A. Salehi, S. Ho, Y. Chen, C. Peng, H. Yersin, F. So, *Adv. Opt. Mater.* **2017**, *5*, 1.
- [42] J. Lee, J. Song, J. Park, S. Yoo, *Adv. Opt. Mater.* **2021**, *2002182*, 1.
- [43] A. Salehi, X. Fu, D. H. Shin, F. So, *Adv. Funct. Mater.* **2019**, *29*, 1.
- [44] T. E. Umbach, S. Röllgen, S. Schneider, H. Klesper, A. M. Umbach, K. Meerholz, *Adv. Eng. Mater.* **2020**, *22*, 1.
- [45] M. Cai, Z. Ye, T. Xiao, R. Liu, Y. Chen, R. W. Mayer, R. Biswas, K.-M. Ho, R. Shinar, J. Shinar, *Adv. Mater.* **2012**, *24*, 4337.
- [46] Y.-F. Liu, J. Feng, Y.-F. Zhang, H.-F. Cui, D. Yin, Y.-G. Bi, J.-F. Song, Q.-D. Chen, H.-B. Sun, *Org. Electron.* **2014**, *15*, 478.
- [47] H.-W. Chang, Y. H. Kim, J. Lee, S. Hofmann, B. Lüssem, L. Müller-Meskamp, M. C. Gather, K. Leo, C.-C. Wu, *Org. Electron.* **2014**, *15*, 1028.
- [48] S.-W. Liu, T.-H. Su, P.-C. Chang, T.-H. Yeh, Y.-Z. Li, L.-J. Huang, Y.-H. Chen, C.-F. Lin, *Org. Electron.* **2016**, *31*, 240.
- [49] S. Ahn, S.-H. Jeong, T.-H. Han, T.-W. Lee, *Adv. Opt. Mater.* **2017**, *5*, 1600512.
- [50] J. Lee, T.-H. Han, M.-H. Park, D. Y. Jung, J. Seo, H.-K. Seo, H. Cho, E. Kim, J. Chung, S.-Y. Choi, T.-S. Kim, T.-W. Lee, S. Yoo, *Nat. Commun.* **2016**, *7*, 11791.
- [51] C.-Y. Wu, M.-H. Ho, S.-Y. Su, C. H. Chen, *J. Soc. Inf. Disp.* **2010**, *18*, 76.

- [52] Z. B. Wang, M. G. Helander, J. Qiu, D. Gao, Y. L. Chang, Z. H. Lu, *Nanotechnology* **2012**, 23, 344010.
- [53] A. Köhnen, M. C. Gather, N. Riegel, P. Zacharias, K. Meerholz, *Appl. Phys. Lett.* **2007**, 91, 3.
- [54] J.-Q. Xi, M. F. Schubert, J. K. Kim, E. F. Schubert, M. Chen, S.-Y. Lin, W. Liu, J. A. Smart, *Nat. Photonics* **2007**, 1, 176.
- [55] J. K. Kim, S. Chhajed, M. F. Schubert, E. F. Schubert, A. J. Fischer, M. H. Crawford, J. Cho, H. Kim, C. Sone, *Adv. Mater.* **2008**, 20, 801.
- [56] M. F. Schubert, D. J. Poxson, F. W. Mont, J. K. Kim, E. F. Schubert, *Appl. Phys. Express* **2010**, 3, 82502.
- [57] J. Kagan, in *Org. Photochem.*, Elsevier, **1993**, pp. 201–221.
- [58] N. Koch, *Phys. status solidi – Rapid Res. Lett.* **2012**, 6, 277.
- [59] W. R. Salaneck, K. Seki, A. Kahn, J.-J. Pireaux, *Conjugated Polymer and Molecular Interfaces: Science and Technology for Photonic and Optoelectronic Application*, CRC Press, **2001**.
- [60] S. Negi, P. Mittal, B. Kumar, *Microsyst. Technol.* **2018**, 24, 4981.
- [61] N. Koch, S. Duhm, J. P. Rabe, A. Vollmer, R. L. Johnson, *Phys. Rev. Lett.* **2005**, 95, 237601.
- [62] J. Guo, N. Koch, S. L. Bernasek, J. Schwartz, *Chem. Phys. Lett.* **2006**, 426, 370.
- [63] A. Yamamori, C. Adachi, T. Koyama, Y. Taniguchi, *Appl. Phys. Lett.* **1998**, 72, 2147.
- [64] J. Blochwitz, M. Pfeiffer, T. Fritz, K. Leo, *Appl. Phys. Lett.* **1998**, 73, 729.
- [65] B. D. Chin, C. Lee, *Adv. Mater.* **2007**, 19, 2061.
- [66] B. W. D'Andrade, S. R. Forrest, *J. Appl. Phys.* **2003**, 94, 3101.
- [67] K. F. H. OR, F. K, J. M, *Chem. Sci. J.* **2016**, 7, DOI 10.4172/2150-3494.1000134.
- [68] K. K. N. S.M.Sze, *Physics of Semiconductor Devices Physics of Semiconductor Devices*, **1995**.

- [69] S. R. Forrest, D. D. C. Bradley, M. E. Thompson, *Adv. Mater.* **2003**, *15*, 1043.
- [70] M. Anaya, B. P. Rand, R. J. Holmes, D. Credgington, H. J. Bolink, R. H. Friend, J. Wang, N. C. Greenham, S. D. Stranks, *Nat. Photonics* **2019**, *13*, 818.
- [71] O. S. Related, **1931**.
- [72] A. C. Harris, I. L. Weatherall, *J. R. Soc. New Zeal.* **1990**, *20*, 253.
- [73] Y. Li, **2019**, 186.
- [74] R. W. G. Hunt, M. R. Pointer, *Measuring Colour*, John Wiley & Sons, **2011**.
- [75] M. C. Gather, S. Reineke, *J. Photonics Energy* **2015**, *5*, 057607.
- [76] T. D. Schmidt, T. Lampe, M. R. Daniel Sylvinson, P. I. Djurovich, M. E. Thompson, W. Brütting, *Phys. Rev. Appl.* **2017**, *8*, 1.
- [77] W. Brütting, J. Frischeisen, T. D. Schmidt, B. J. Scholz, C. Mayr, *Phys. Status Solidi Appl. Mater. Sci.* **2013**, *210*, 44.
- [78] M. Furno, R. Meerheim, S. Hofmann, B. Lüssem, K. Leo, *Phys. Rev. B - Condens. Matter Mater. Phys.* **2012**, *85*, 1.
- [79] S. Y. Kim, W. I. Jeong, C. Mayr, Y. S. Park, K. H. Kim, J. H. Lee, C. K. Moon, W. Brütting, J. J. Kim, *Adv. Funct. Mater.* **2013**, *23*, 3896.
- [80] J. Frischeisen, D. Yokoyama, A. Endo, C. Adachi, W. Brütting, *Org. Electron.* **2011**, *12*, 809.
- [81] K. H. Kim, C. K. Moon, J. H. Lee, S. Y. Kim, J. J. Kim, *Adv. Mater.* **2014**, *26*, 3844.
- [82] M. Flämmich, J. Frischeisen, D. S. Setz, D. Michaelis, B. C. Krummacher, T. D. Schmidt, W. Brütting, N. Danz, *Org. Electron.* **2011**, *12*, 1663.
- [83] L. H. Smith, J. A. E. Wasey, I. D. W. Samuel, W. L. Barnes, *Adv. Funct. Mater.* **2005**, *15*, 1839.
- [84] R. Meerheim, M. Furno, S. Hofmann, B. Lüssem, K. Leo, *Appl. Phys. Lett.* **2010**, *97*, 28.
- [85] M. Furno, R. Meerheim, M. Thomschke, S. Hofmann, B. Lüssem, K. Leo, *Light. Diodes Mater. Devices, Appl. Solid State Light. XIV* **2010**, 7617,

- 761716.
- [86] M. H. Lu, J. C. Sturm, *J. Appl. Phys.* **2002**, 91, 595.
- [87] S. Nowy, J. Frischeisen, W. Brütting, *Org. Light Emit. Mater. Devices XIII* **2009**, 7415, 74151C.
- [88] S. Nowy, B. C. Krummacher, J. Frischeisen, N. A. Reinke, W. Brütting, *J. Appl. Phys.* **2008**, 104, DOI 10.1063/1.3043800.
- [89] J.A Woollam Co., Inc. CompleteEASE Software Manual.
- [90] D. D. Zhang, J. L. Xu, H. B. Sun, *Adv. Opt. Mater.* **2021**, 9, 1.
- [91] J. H. Kim, J. W. Han, D. J. Lee, S. A. N. Entifar, Z. R. Ramadhan, K. T. Lim, Y. H. Kim, *Org. Electron.* **2018**, 54, 204.
- [92] D. T. F. Marple, *J. Appl. Phys.* **1964**, 35, 1241.
- [93] M. Raihane, B. Ameduri, **2014**, 453.
- [94] M. Vasilopoulou, A. M. Douvas, L. C. Palilis, P. Bayiati, D. Alexandropoulos, N. A. Stathopoulos, P. Argitis, *Microelectron. Eng.* **2009**, 86, 1142.
- [95] Z. Yang, H. Peng, W. Wang, T. Liu, *J. Appl. Polym. Sci.* **2010**, 116, 2658.
- [96] J. Liang, E. Toussaere, R. Hierle, R. Levenson, J. Zyss, A. V. Ochs, A. Rousseau, B. Boutevin, *Opt. Mater. (Amst)*. **1998**, 9, 230.
- [97] K. Landfester, N. Bechthold, F. Tiarks, M. Antonietti, *Macromolecules* **1999**, 32, 5222.
- [98] L. L. Hecht, C. Wagner, K. Landfester, H. P. Schuchmann, *Langmuir* **2011**, 27, 2279.
- [99] H. J. Lehmle, *Chemosphere* **2005**, 58, 1471.
- [100] S. Banerjee, J. Schmidt, Y. Talmon, H. Hori, T. Asai, B. Ameduri, *Chem. Commun.* **2018**, 54, 11399.
- [101] A. H. Ribeiro, A. Fakih, B. Van Der Zee, L. Veith, G. Glaser, A. Kunz, K. Landfester, P. W. M. Blom, J. J. Michels, *J. Mater. Chem. C* **2020**, 8, 6528.
- [102] F. J. M. Colberts, M. M. Wienk, R. A. J. Janssen, *ACS Appl. Mater. Interfaces* **2017**, 9, 13380.

-
- [103] Y. H. Kim, J. Lee, W. M. Kim, C. Fuchs, S. Hofmann, H.-W. Chang, M. C. Gather, L. Müller-Meskamp, K. Leo, *Adv. Funct. Mater.* **2014**, *24*, 2553.
- [104] C. Lee, D. J. Kang, H. Kang, T. Kim, J. Park, J. Lee, S. Yoo, B. J. Kim, *Adv. Energy Mater.* **2014**, *4*, 1301345.
- [105] H. Jiang, W. Zhao, C. Li, Y. Wang, *Polymer (Guildf)*. **2011**, *52*, 778.
- [106] Y. Li, N. B. Kotadiya, B. van der Zee, P. W. M. Blom, G. J. A. H. Wetzelaer, *Adv. Opt. Mater.* **2021**, *9*, 1.
- [107] S. Höfle, A. Schienle, M. Bruns, U. Lemmer, A. Colmann, *Adv. Mater.* **2014**, *26*, 2750.

List of Figures

Figure 2.1. Examples of external outcoupling structures.	4
Figure 2.2. ^[31] Schematic illustration of a patterned ITO with the low-index conductive PEDOT:PSS used to extract light from waveguide mode in an OLED.	5
Figure 3.1. ^[57] Scheme of the main steps involved in the process of light emission in an OLED.	7
Figure 3.2. ^[13] The energy diagram of a typical multilayer OLED.....	8
Figure 3.3. ^[67] Schematic structures of (a) Bottom-emitting OLEDs, (b) Top- emitting OLEDs.....	8
Figure 3.4. ^[73] (a) Three color matching functions. (b) The CIE1931 xy chromaticity diagram.....	11
Figure 3.5. ^[75] Illustration of refraction of the light emitted in the emissive layer (EML) of a bottom-emitting OLED.....	14
Figure 3.6. ^[76] Schematic illustration of an oscillating electrical dipole embedded in a dielectric layer.	14
Figure 3.7. ^[43] Effect of dipole orientation on mode-contribution in an OLED device.	15
Figure 3.8. (a) ^[42] Schematic diagram of the device structure of a bottom emitting OLED with ray tracing to demonstrate various modes in OLEDs. (b) ^[84] Quantification of different loss channels for a red bottom emitting OLED.....	16
Figure 4.1. ^[89] Interaction of polarized light with a sample.	22
Figure 4.2. ^[89] Schematic of (a) physical surface roughness; (b) optical model of surface roughness.	22
Figure 5.1. Chemical structure of (a) PFPA (pentafluorophenyl acrylate), (b) 4H- PFDA (1H,1H,2H,2H-perfluorodecyl acrylate), (c) V59 (2,2'-Azobis(2- methylbutyronitrile)), (d) PFOS (perfluorooctanesulfonic acid) and (e) SDS (sodium dodecyl sulfate).	26

Figure 5.2. Chemical structure of PEDOT:PSS.....	26
Figure 5.3. (a) NP3-PEDOT:PSS blend film spin-coated on Si substrate. (b) NP5-PEDOT:PSS blend film spin-coated on Si substrate.....	28
Figure 5.4. Refractive indices spectra of PEDOT:PSS and NP5-PEDOT:PSS thin films.....	28
Figure 5.5. AFM images of (a) PEDOT:PSS film, (b) and (c) NP5-(PEDOT:PSS) film.	29
Figure 5.6. AFM images of (a) and (b) PS(30 nm)-PEDOT:PSS (1:1). (c) and (d) PS(100 nm)-PEDOT:PSS (1:1). (e) and (f) PS(100 nm)-PEDOT:PSS (1:3).	31
Figure 5.7. Refractive indices (n) spectra of PEDOT:PSS, the blends PS(30nm)-PEDOT:PSS (1:1), PS(100nm)-PEDOT:PSS (1:1) and PS(100nm)-PEDOT:PSS (1:3) thin films.....	32
Figure 5.8. Transmittance spectra of PEDOT:PSS layer and the porous PEDOT:PSS layers.....	33
Figure 5.9. Device performance of OLEDs.	34
Figure 5.10. (a) OLED structure for the simulation. (b) The result of optical simulation.....	35
Figure 6.1. ^[107] (a) Inverted OLED device structure. (b) Proposed energy levels of the OLED.	38
Figure A.1. A TGA curve of (a) poly(pentafluorophenyl acrylate), (b) poly(1H,1H,2H,2H-Perfluorodecylacrylat).	49
Figure A.2. The fitting of experimental ellipsometric data.	50

List of Tables

Table 2.1.⁸ Maximum Achievable Air (η_A) and Air + Substrate (η_{A+S}) *EQEs*6

Table 5.1. Synthesis of fluorinated polymer nanoparticles via mini-emulsion polymerization.....25

A. Appendix

In this chapter, some supplemental data are presented.

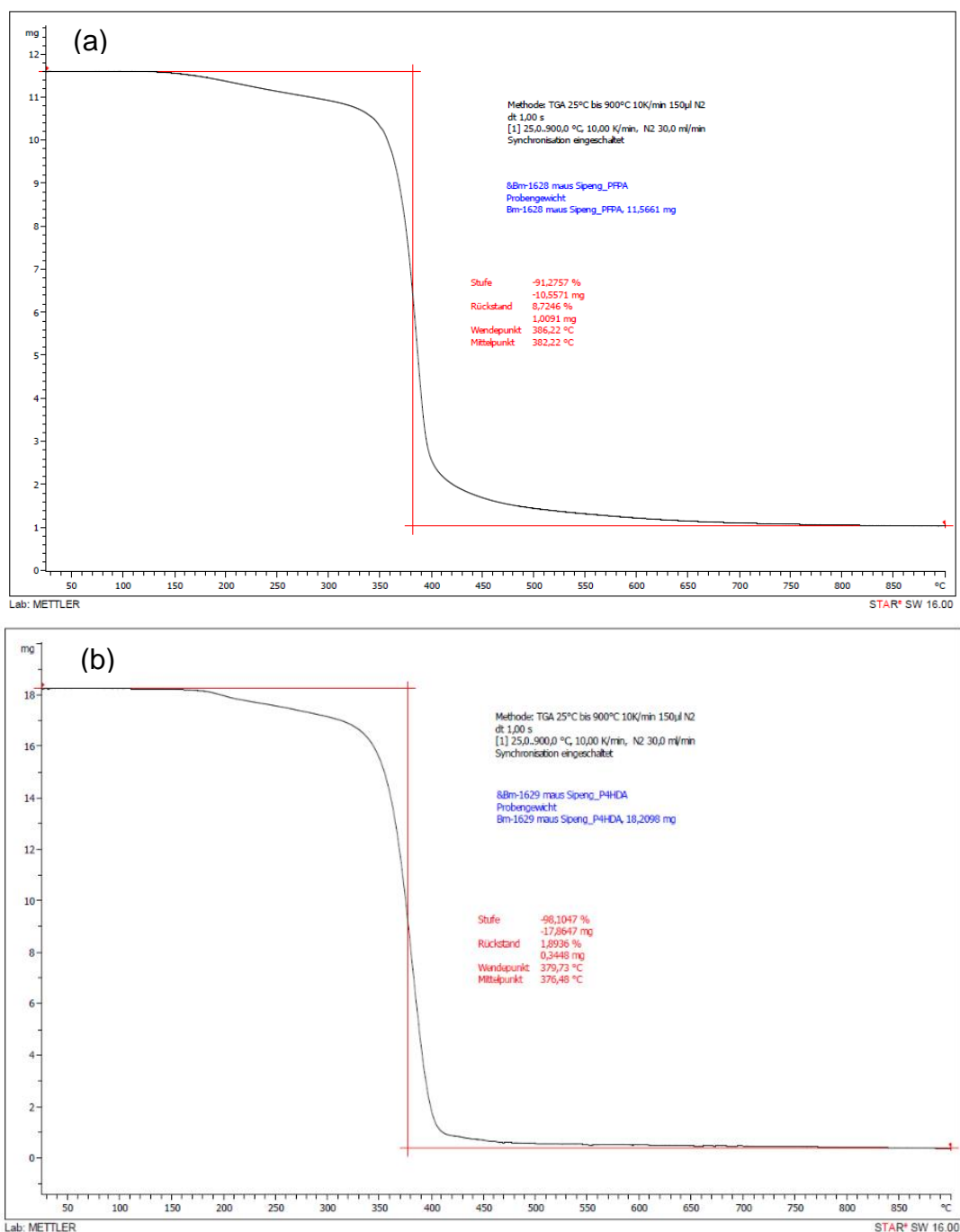


Figure A.1. A TGA curve of (a) poly(pentafluorophenyl acrylate), (b) poly(1H,1H,2H,2H-Perfluorodecylacrylat). Both fluorinated polymer exhibit relative good thermal stability, as they start to decompose at around 300 °C.

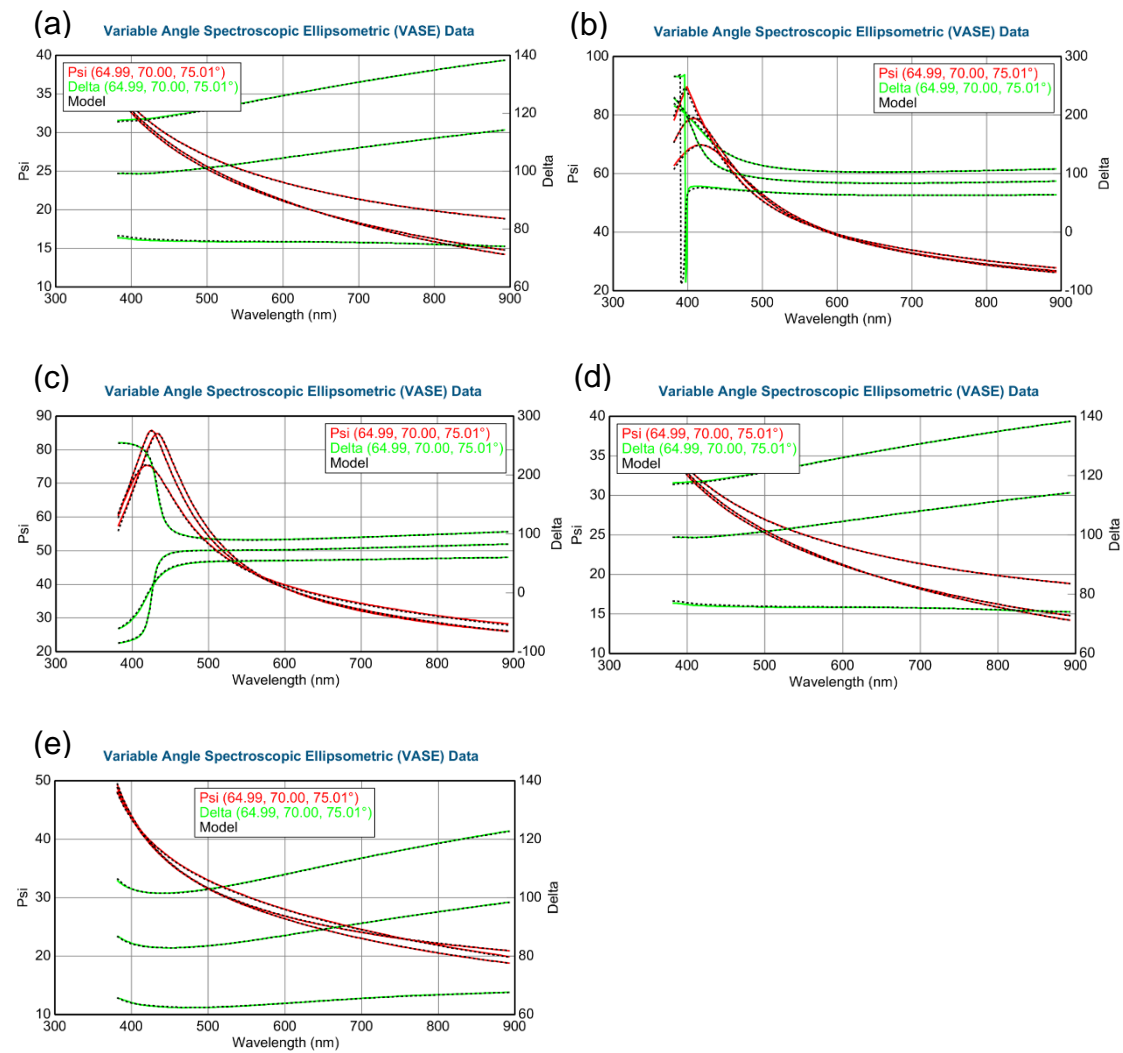


Figure A.2. Experimental (solid lines) and the fitted (dashed lines) ellipsometric parameters, Psi (red lines) and Delta (green lines), of (a) pristine PEDOT:PSS layer, (b) NP5-PEDOT:PSS layer, (c) PS(30nm)-PEDOT:PSS (1:1) layer, (d) PS(100nm)-PEDOT:PSS (1:1) layer, and (e) PS(100nm)-PEDOT:PSS (1:3) layer. Good agreement was found between the measured and fitted data in the visible wavelength region in each case.

B. Acknowledgements

First of all, I would like to thank Prof. Bernhard Rieger and Dr. Gert-Jan Wetzelaer for being my supervisors and giving me the opportunity to write my Master's Thesis at the Max-Planck-Institute for Polymer Research.

I would like to acknowledge Dr. Yungui Li for his helpful suggestions and sharing many helpful python scripts.

I would like to thank all the members in AK Blom for the pleasant atmosphere and especially Prof. Paul Blom, Dr. Jasper Michels, Xiao Tan, Davis Trieb, Oskar Sachnik, Yilsiz Okan for their advises to my experiments.

I would like to thank all the technicians in AK Blom. I am grateful for the help of Christian Bauer, Hans-Jürgen Guttman and Frank Keller in case of technical problems. I also appreciate the support by Verona Maus to the TGA measurement.

I would also like to thank Prof. Katharina Landfester and Katja Klein for the suggestions and support to the mini-emulsion synthesis.

Finally, I would like to thank my parents, my friends and my girlfriend for all the support, encouragement and care throughout my years of study and the process of researching and writing this thesis.

C. Statement of Authorship

Erklärung

Ich versichere hiermit, dass ich die von mir eingereichte Abschlussarbeit selbstständig verfasst und keine anderen als die angegebenen Quellen und Hilfsmittel benutzt habe.

München, 30.09.2021, Sipeng Liu

Ort, Datum, Unterschrift

Declaration of Independent Work

I hereby declare that I have independently written this thesis and have not used any other references and resources than those mentioned.

München, 30.09.2021, Sipeng Liu

Place, Date, Signature